QATAR UNIVERSITY

COLLEGE OF ARTS AND SCIENCES

FABRICATION OF HETEROSTRUCTURED TiO_2 NANORODS FOR ENHANCED SOLAR WATER SPLITTING

BY

FADI ZAFER KAMAND

A Thesis Submitted to

the College of Arts and Sciences

in Partial Fulfillment of the Requirements for the Degree of

Master of Science in Materials Science and Technology

June 2020

COMMITTEE PAGE

The members of the Committee approve the Thesis of
Fadi Zafer Kamand defended on 22/04/2020.

Dr. Talal Altahtamouni
Thesis Supervisor

Dr. Aboubakr M. Abdullah
Committee Member

Dr. Siham Al-Qaradawi
Committee Member

Dr. Nasr Bensalah
Committee Member

Approved:

Ibrahim AlKaabi, Dean, College of Arts and Sciences

ABSTRACT

KAMAND, FADI, ZAFER, Masters: April: 2020, Materials Science and Technology

Title: Fabrication of Heterostructured TiO_2 Nanorods for Enhanced Solar Water Splitting

Supervisor of Thesis: Dr. Talal, M., Altahtamouni.

As global population growth and energy demand keep to ramp up, green and sustainable energy production with environmental concerns has become as one of the most serious challenges over the past years. Photocatalysis is a promising approach and can be regarded as a green and efficient energy source. Up to date, TiO_2 has been demonstrated as one of the most used photocatalytic materials for photoelectrochemical (PEC) water splitting due to its low-cost, non-toxicity, high chemical and physical stabilities, and the excellent photocatalytic properties. However, TiO_2 exhibits drawbacks such as high rate of electron-hole recombination and wide band gap, which means only ~4% of the solar spectrum can be absorbed to promote charge carrier generation in the material. In order to overcome these limitations, various strategies have been developed to improve its photocatalytic activity toward the solar-driven water splitting including nanostructured morphology engineering, and construction of heterostructures. One-dimensional (1D), 2D TiO_2 nanostructures exhibit unique PEC properties due to the faster charges transfer, and lower charges recombination rate. Oxynitrides are class of semiconducting materials that exhibits a good photocatalytic activity. However, the fast rate of the charges recombination and the bandgap edges can limit their usage as an efficient photocatalysts. Fabrication of heterostructure can be efficient approach to enhance the PEC water splitting. The novel $LaMo(ON)_x/TiO_2$ heterostructure (is not reported in the literature before) was synthesized via two-step procedure. In the first

step, TiO_2 nanorods (NRs) were prepared using hydrothermal synthesis. After that, $LaMo(ON)_x$ was deposited on the as-fabricated TiO_2 NRs by electrophoretic deposition. The characterization techniques signified that heterojunction structure of $LaMo(ON)_x$ deposited on TiO_2 NRs arrays were formed. The various characterization techniques revealed that the heterojunction preserved the nanorods morphology of pristine TiO_2 NRs. The fabricated heterostructure was characterized using scanning electron microscope (SEM), X-Ray diffraction (XRD), Raman spectroscopy and X-ray photoelectron spectroscopy (XPS). The photoelectrochemical measurements showed more than doubled enhancement in the photocurrent density of the heterostructure compared to the pristine TiO_2 NRs. This was attributed to the efficient electron-hole (e^--h^+) charge separation at the interface of heterojunction which increases the life time of the photoinduced e^--h^+ pairs, and enhance the PEC activity.

DEDICATION

This work is dedicated to my family and my wife who have always been the inspiring and supporting people behind of my whole successes in this life.

ACKNOWLEDGMENTS

This work becomes a reality with the kind support of many people whose names may not all be enumerated. I would like to express my sincere thanks to all those who helped me with their appreciated support during the entire process of this thesis.

I would like to acknowledge my indebtedness and render my warmest thanks to my supervisor, Dr. Talal Altahtamouni, who made this work possible. He was always supportive and helpful throughout all stages of the work. In addition, he was the first one who was helping to solve the faced issues during around two years. His valuable comments and suggestions helped me a lot to build my researcher personality. I really thank him for imparting his knowledge and expertise in this thesis.

I would like to express my gratitude to the thesis committee members, Dr. Aboubakr M. Abdullah, Dr. Siham Al-Qaradawi, and Dr. Nasr Bensalah because this work has benefited from their suggestions and comments. Thank you all for the valuable approval of my work and exemplary recognition.

My sincere thanks are for Dr. Tran Nam Trung, who taught me the preparation techniques, the methodology, and the scientific approach to conduct this research work. I appreciate his kindness, patience and generosity because he spent long time to train me and to improve my critical thinking skills.

I would express my gratitude to Dr. Yahia Shoeb for his valuable time spent with me and extended discussions, which had contributed to increase the quality of this work.

Special thanks are due my parents who have taught me the love of sciences, and who were the main source of inspiration. I want to thank my grandmother, as well as my brothers Rajeh and Beshr for their continuous encouragement and helping me in my

daily life issues, which helped me to complete this research. My thanks are extended to my beloved and supportive wife Dr. Fatima Ajaj for her patience and continuous support, not only that but also for many valuable efforts to offer great and quiet environment in our lovely home. .

The people with the greatest indirect contribution to this thesis are my friends, colleagues, and relatives who were kept motivating me and provide any needed support to help me for overcoming any issue.

TABLE OF CONTENTS

DEDICATION v

ACKNOWLEDGMENTS vi

LIST OF TABLES xi

LIST OF FIGURES xii

Chapter 1: INTRODUCTION 1

1.1. Semiconductors and absorption of light 4

1.2. Solar driven water splitting process 5

1.3. The requirements of the good photoelectrode 6

1.3.1. Light absorption and bandgap 6

1.3.2. Chemical stability 7

1.3.3. Suitable positions of the band edges 7

1.3.4. Efficient charge transport 8

1.4. TiO_2 properties as photoelectrode 8

1.4.1. The structural properties of TiO_2 8

1.4.2. The electronic properties of TiO_2 9

1.5. TiO_2 photocatalyst drawbacks 10

1.6. TiO_2 photocatalyst performance enhancement approaches 11

1.6.1. Nanostructure morphologies 11

1.6.2. Coupling with heterostructures 11

1.7. Heterojunctions with TiO_2 12

1.7.1. Band alignment in heterojunctions 13

CHAPTER 2: LITRETURE REVIEW 15

Chapter 3: EXPERIMENTAL 23

3.1. Materials 23

3.2. Material Preparation 23

3.2.1. Synthesis of TiO_2 nanorods 23

3.2.2. Thermal treatment 25

3.2.3. Preparation of $LaMo(ON)_x$ 25

3.2.4. Preparation of $LaMo(ON)_x/TiO_2$ heterostrostructure 25

3.3. Photoelectrochemical measurements 26

3.4. Material characterization and Equipment 28

3.4.1. Scanning electron microscope (SEM) 28

3.4.2. Raman spectroscopy 30

1.4.3. X-Ray diffraction 31

1.4.4. X-ray photoelectron spectroscopy (XPS) 32

1.4.5. UV-Vis spectroscopy 33

CHAPTER 4: RESULTS AND DISCUSSION 35

4.1. Fabrication of TiO_2 nanorods 35

4.1.1. The effect of growth temperature 35

4.1.2. The effect of growth time 38

4.1.3. The effect of HCl:Ti volume ratio 41

4.2. Characterization of pristine TiO_2 44

4.3. Heterostructure fabrication 51

4.4. Characterization of the $LaMo(ON)_x$/ TiO_2 heterostructure 52

4.6. Photoelectrochemical performance 56

CHAPTER 5: CONCLUSION 62

FUTURER WORK 63

REFERENCES 64

LIST OF TABLES

Table 1. List of Several Dopants Types Used for TiO_2 Doping. 17

Table 2. Summary of PEC Experimental Results for the Effect of Temperture. 38

Table 3. Summary of PEC Experimental Results for the Effect of Time. 40

Table 4. Summary of PEC Experimental Results for Effect of the HCl:Ti Volume: Ratio.... 43

Table 5. Optimized Synthesis Conditions of TiO_2 NRs..... 44

Table7. The Maximum Frequency and Electron Life Time of TiO_2 and $LaMo(ON)_x/TiO_2$. .. 60

LIST OF FIGURES

Figure 1. Renewable and non-renewable techniques for H_2 production[8].....3

Figure 2: Schematic diagram of photocatalytic water splitting process[16].....6

Figure 3. The bandgap edges positons with respect to RHE and the water redox energy levels[19].....7

Figure 4. The unit cell of the TiO_2 crystalline phases (the most common)[27].....9

Figure 5. illustration shows the band structure of (a) direct and (b) indirect gap semiconductors.....10

Figure 6. Band diagram that shows the three possible band alignment types: (a) type I (b) typeII (c) type III[53].....13

Figure 7. Illustration of Teflon-lined stainless steel autoclave.....24

Figure 8. Illustration of the electrophoretic deposition preparation process.....26

Figure 9. Illustration of quartz three-electrode system of PEC measurements.....28

Figure 10. Schematic diagram of the interactions between the sample surface and the primary electron beam.....29

Figure 11. A schematic diagram shows the scattering types of Raman spectroscopy 31

Figure 12. Schematic view of Bragg's law.....32

Figure 13. A schematic diagram of the XPS instrument.....33

Figure 14. UV-Vis experimental setup of the transmittance and the reflectance measurements.....34

Figure 15. Top-view SEM images of TiO_2 NRs fabricated at: (a) 140 °C (b) 160 °C (c) 180 °C and cross-sectional SEM images of TiO_2 NRs fabricated at: (d) 140 °C (e) 160 °C (f) 180 °C.....36

Figure 16. PEC measurements of TiO_2 fabricated at 140 °C, 160°C, and 180 °C: (a)

Linear sweep voltammograms under light (b) Nyquist impedance plots of different electrodes recorded at 0.8 V vs. Ag/AgCl in 1 M KOH. (c) Amperometric on-off curve at 0.8 V vs Ag/AgCl with light on/off cycles 37

Figure 17. Top-view SEM images of TiO_2 NRs prepared at different growth period : (a) 6 h (b) 10 h (c) 14 h and cross-sectional SEM images of TiO_2 NRs prepared at different growth period: (d) 6 h (e) 10 h (f) 14 h 39

Figure 18. PEC measurements of TiO_2 fabricated at 6h, 10h, and 14h: (a) Linear sweep voltammograms under light (b) Nyquist impedance plots of different electrodes recorded at 0.8 V vs. Ag/AgCl in 1 M KOH. (c) Amperometric on-off curve at 0.8 V vs Ag/AgCl with light on/off cycles 40

Figure 19. Top-view SEM images of TiO_2 NRs prepared at different HCl: Ti volume ratios : (a) 40:1 (b) 50:1 (c) 60:1 and cross-sectional SEM images of TiO_2 NRs prepared at different growth period: (d) 40:1 (e) 50:1 (f) 60:1. 41

Figure 20. PEC measurements of TiO_2 fabricated using HCl:Ti volume ratios: 40:1, 50:1, and 60:1: (a) Linear sweep voltammograms under light (b) Nyquist impedance plots of different electrodes recorded at 0.8 V vs. Ag/AgCl in 1 M KOH (c) Amperometric on-off curve at 0.8 V vs Ag/AgCl with light on/off cycles 43

Figure 21. SEM images of the as-fabricated TiO_2 NRs: (a) top view, (b) cross-sectional, (c) SEM-EDX spectrum of the as-fabricated TiO_2 45

Figure 22. XRD pattern of the as-fabricated rutile TiO_2 46

Figure 23. Raman spectra of the pristine rutile TiO_2.....48

Figure 24. XPS spectra of pristine TiO_2: (a) XPS survey spectra, high-resolution XPS spectra of (b) Ti 2p and (c) of O 1s.....50

Figure 25. The UV-Vis absorbance spectrum of TiO_2. The inset shows the plot of

$(Ah\nu)^2$ versus energy ($h\nu$) for TiO_2 51

Figure 26. The SEM top view images of (a) pristine TiO_2, (b) $LaMo(ON)_X$, (c) $LaMo(ON)_X$/ TiO_2 (D) SEM-EDX spectrum of $LaMo(ON)_x/TiO_2$ heterostructure 53

Figure 27. XRD patterns of pure TiO_2, $LaMo(ON)_x$, and $LaMo(ON)_x/TiO_2$ heterostructure 54

Figure 28. Raman spectra of pristine TiO_2 (black) and $LaMo(ON)_x/TiO_2$ (red) 55

Figure 29. XPS spectra of $LaMo(ON)_x/TiO_2$ heterostructure: (a) XPS survey spectra and the high resolution XPS spectra of (b) La 3d (c) of Mo 3d (d) O 1s (e) Ti 2p and (f) N 1s 56

Figure 30. (a) The linear sweep voltammograms of pristine TiO_2 and $LaMo(ON)_x/TiO_2$ (b) Tafel plots of TiO_2 and $LaMo(ON)_x/TiO_2$ (c) Nyquist impedance plots of TiO_2 and $LaMo(ON)_x/TiO_2$ recorded at 0.8 V vs. Ag/AgCl in 1 M KOH. (d) Amperometric on-off curve of TiO_2 and $LaMo(ON)_x/TiO_2$ at 0.8 V vs Ag/AgCl with light on/off cycles 58

Figure 31. (a) Bode phase plot of pristine TiO_2 and $LaMo(ON)_x/TiO_2$ 59

Figure 32. Schematic diagram photocatalytic mechanism of the $LaMo(ON)_x/TiO_2$ heterostructure under light 60

CHAPTER 1: INTRODUCTION

As global population growth and energy demand keep to ramp up, green and sustainable energy production with environmental concerns has become as one of the most serious challenges over the past years. Thus, the huge increase in the human population and the growth in the industrial development result in continuous increase in the need of the limited sources of energy. Renewable energy development is highly needed for offering alternative energy resources that are environmentally friendly. The utilization of traditional fossil fuels led to dramatic increase in the atmospheric CO_2 emissions that harm the environment as well as living species[1]. Consequently, great efforts have been devoted to develop renewable sources that substitute fossil fuels such as wind, biomass and solar energy.

Among the variety of renewable energy resources, solar energy is the most abundant source on the earth. The radiation of the sun deposits on the Earth planet around 120,000 TW of radiation, which is covering more than the human energy requirement as in the highest energy demand scenarios[2]. It was reported that the amount of the global utilization energy used was 18 TW in 2015[3]. However, due to the climate and seasonal variations of the sunlight, solar energy can be utilized through conversion to another energy form such as chemical fuels or transferring systems, which allows the usage, storage, and transportation of the energy when it is required[4]. Solar energy is highly abundant clean source of energy that can be used to generate H_2 gas through water electrolysis:

$$H_2O_{(l)} \longrightarrow \frac{1}{2} O_{2\,(g)} + H_{2\,(g)}$$

To facilitate the above reaction, the system should be provided with energy that can break the H_2O molecule (ΔG= 237 kJ/mol) using electricity which requires in turn the combustion of hydrocarbon fuels to be generated[5].

Hydrogen (H_2) is one of the most attractive energy carriers as it provides an efficient and clean conversion of chemical energy into electrical via a fuel cell and it produces water as the only by-product. Therefore, the usage of hydrogen as a fuel have unbeatable advantage of decreasing the emissions of greenhouse gases to the mother nature. H_2 is used as green fuel due to its high energy yield (around 122 kJ/g) that is almost three times more than the hydrocarbon fuels, and its utilization generates only water vapor, which prevents the emissions of greenhouse gases to the environment that could be produced upon the utilization of the hydrocarbon fuels[1]. However, the industrial production of H_2 produces large amounts of side products such as greenhouse gases and it consumes a lot of energy required for heating and reaching high temperatures, which is costly. Several techniques used to produce hydrogen are illustrated in Figure 1. To show an example about the major differences between the non-renewable and renewable hydrogen production, steam-reforming technique, which is widely used on the industrial scale for production of H_2, would be shown in terms of the following chemical equations:

$$\mathrm{CH_4} + \mathrm{H_2O} \rightleftharpoons \mathrm{CO} + 3\mathrm{H_2} \qquad \Delta H_f^\circ = 206\ \mathrm{KJ/mol} \quad (1.1)$$

$$\mathrm{CO} + \mathrm{H_2O} \rightleftharpoons \mathrm{CO_2} + \mathrm{H_2} \qquad \Delta H_f^\circ = -41\ \mathrm{KJ/mol} \quad (1.2)$$

As shown in reaction 1.1, the endothermic reaction requires high temperatures (around 1000 °C) to convert the methane (non-renewable source) of hydrogen. In addition, the CO will be formed as a product, which will shift reaction 1.2 to the completion, CO_2, the greenhouse gas, is generated in the reaction as a by-product, which contributes to the global warming. On the other hand, H_2 can be produced in sustainable way without deleterious emissions to the environment by the splitting of water (reaction 1.3) assisted by the solar energy[6]:

$$H_2O\,(l) \rightleftharpoons \frac{1}{2}\,O_2\,(g) + H_2(g) \qquad \Delta G_f^{\circ} = 237\ \text{KJ/mol} \quad (1.3)$$

The electrolysis of water requires providing an electricity to the reaction, which is non-renewable approach due to the need to produce the electricity from fossil raw materials. So, the solar radiations can be used to facilitate the above reaction renewably (photoelectrolysis)[7].

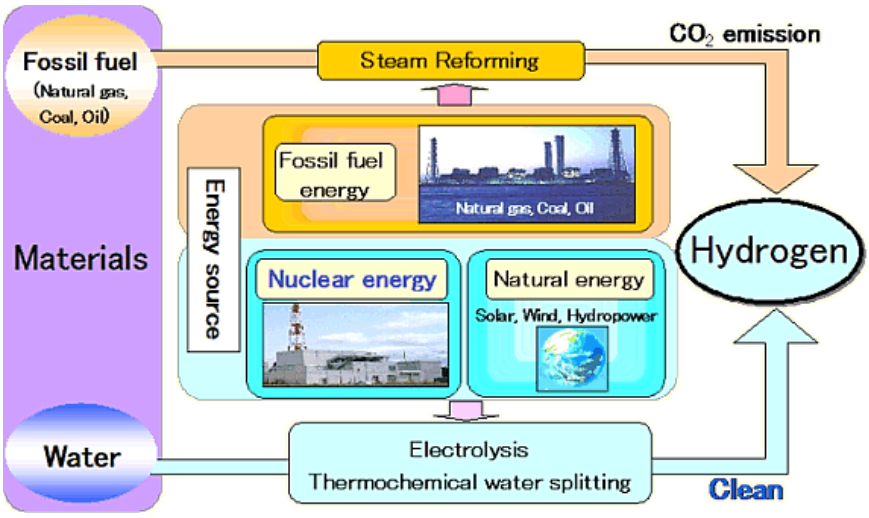

Figure 1. Renewable and non-renewable techniques for H_2 production[8]

Photocatalysis is a promising approach and can be regarded as a green and efficient method to accelerate a photoreaction. The photocatalytic process is taking place at the surface of semiconducting materials under the irradiation of photons. Photocatalysis process is the core-needed concept required for renewable energy generation such as water splitting for hydrogen production[9]. Photocatalysis terminology is referred to the process of the initiation and the acceleration of the photoreaction upon irradiation of light at a photocatalyst. The word photo- is added to the word catalyst because the catalyst active sites are not active in the dark and the activation of the reaction sites will happen only under light illumination. Furthermore, the density of the

active sites plays a major role in the catalytic activity; and in addition, the intensity of the irradiated light is a major key that determines the reaction rate[4].

1.1. Semiconductors and absorption of light

Semiconductors are materials with an energy bandgaps (E_g) smaller than the insulators and larger than the conductors, which can help the electrons upon the excitation to jump from the valance band to the conduction band, and to form photogenerated charges of electron hole (e-h) pairs. Semiconductor materials exhibit an energy band with a distinction between the valance band (VB) and the conduction band (CB) separated by the forbidden bandgap (E_g), in which no available states are existed[10]. When a semiconductor photcatalyst absorbs the appropriate amount of energy (equals or larger than E_g) from the light photon, the electrons (e^-) in the VB get excited to the CB and leaves the positively charged holes (h^+) in the VB[10,4]. Consequently, when the photogenerated electrons are capable to be consumed externally (not locally on the semiconductor surface) through an electrical circuit, an electrical current can be produced and used as an energy source toward water splitting or electricity generation.

The process of the photogeneration of (e-h) pair from a semiconductor photocatalyst may be summarized as in the following equation:

$$2\,hv \longrightarrow 2\,e^- + 2\,h^+ \qquad (1.4)$$

Where *h* is Planck's constant, and *v* is the frequency of photon.

The photoexcitation of electrons and holes causes the oxygen evolution reaction (OER) which is oxidation of water by the holes (reaction 1.5), while the hydrogen evolution reaction (HER) is caused by the reaction of the electrons with H^+ ions (reaction 1.6). The water splitting overall reaction is the combination of the OER and HER half reactions (reaction 1.7)[10].

$$H_2O + 2h^+ \rightleftharpoons 2H^+ + \frac{1}{2}O_2(g) \qquad E^\circ_{ox,an} = -1.229\ \text{V vs. SHE} \quad (1.5)$$

$$2H^+ + 2e^- \rightleftharpoons H_2(g) \qquad E^\circ_{red,cat} = 0\ \text{V vs. SHE} \quad (1.6)$$

$$H_2O \rightleftharpoons \frac{1}{2}O_2(g) + H_2(g) \qquad \Delta E^\circ = E^\circ_{red,cat} + E^\circ_{ox,an} \approx -1.23\ \text{V} \quad (1.7)$$

Relative to the standard hydrogen electrode (SHE), the electrode potential for the anodic reaction is negative and the electrode potential for the cathodic reaction is zero. Consequently, the total cell potential (ΔE°) equals -1.23 V, which is the minimum voltage needed for the water splitting reaction; in addition, the negative electrochemical cell voltage indicates that the reaction is non-spontaneous and requires adding energy to occur [11]. For water splitting, the band energy edges (CB and VB) of a semiconductor must straddle the redox potentials to enable the charge carriers to initiate redox reactions. The conduction band minimum (or E_C) must has higher energy level and lower electrochemical potential than the HER potential, and the valance band maximum (or E_V) must be less in energy level and more in electrochemical potential than the OER potential. However, the actual potential needed for the water splitting reaction to take place is more than 1.23 V due to the thermodynamic losses of 0.3-0.4 V[12], and 0.4 - 0.6 V applied overpotential to guarantee fast reaction rate[13], which means that the minimum actual potential (or bandgap of semiconductor) requisite for water splitting reaction is around 1.9 - 2.2 V[14].

1.2. Solar driven water splitting process

Water can be decomposed through photoelectrolysis or photoelectrochemical (PEC) water splitting. In order to promote the water splitting reaction, a semiconductor material is required to play the role of the photocatalyst, which captures the energy from the solar radiations, and deliver it to the water molecules to be decomposed at separated electrodes[15]. During the illumination of light, and when the semiconductor material

absorbs energy from the photons equal or higher than the energy bandgap, the semiconductor material generates electron-hole pair (as described previously). The photogenerated species play the role of oxidizing and reducing agents where the electrons will reduce the water molecules to produce the H_2 gas, and the holes oxidizes the water to evolve the oxygen gas (as illustrated in Figure 2).

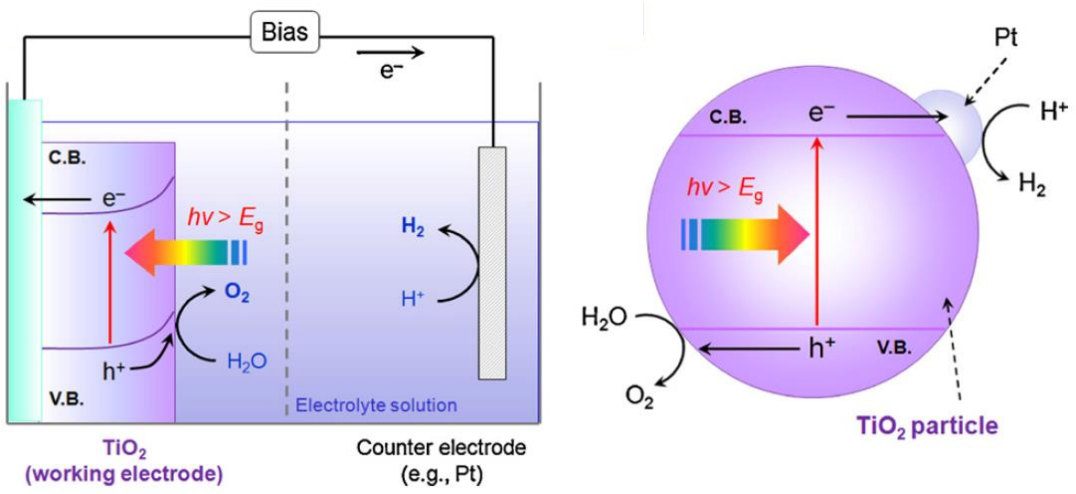

Figure 2: Schematic diagram of photocatalytic water splitting process[16]

1.3. The requirements of the good photoelectrode

To design a high performance PEC cell, an efficient photoelectrode material is needed. In addition to the high electrical conductivity and low resistance features, low cost, and using the appropriate substrate[17], the photoelectrode should have several properties for efficient photoelectrochemical water splitting[18]:

1.3.1. Light absorption and bandgap

The bandgap is responsible for indicating the spectral region of the light absorption of the semiconductor materials and it shows the minimum amount of energy required to excite the electron from the VB to the CB[14].

1.3.2. Chemical stability

It is very important for the good photoelectrode to resist the solid/liquid interface chemical reactions because these reactions can cause a degradation (dissolution, photo- and electrochemical corrosion) of the photoelectrode[9].

1.3.3. Suitable positions of the band edges

Another needed feature for a semiconductor to perform PEC water splitting is the CB and VB energy levels in comparison with the H_2O oxidation and reduction potential values. The energy of the CB should be lower than energy potential of the oxidation of oxygen to water (O_2/H_2O), and the valance band edge energy should be higher than the reduction potential value of hydrogen ions to hydrogen (H^+/H_2)[18]. The illustration in Figure 3 shows several semiconductors band edges (using RHE as a reference electrode) in comparison with the H_2O redox energy levels. It can be seen that there are limitations toward using the semiconductor materials as photoelectrodes[19].

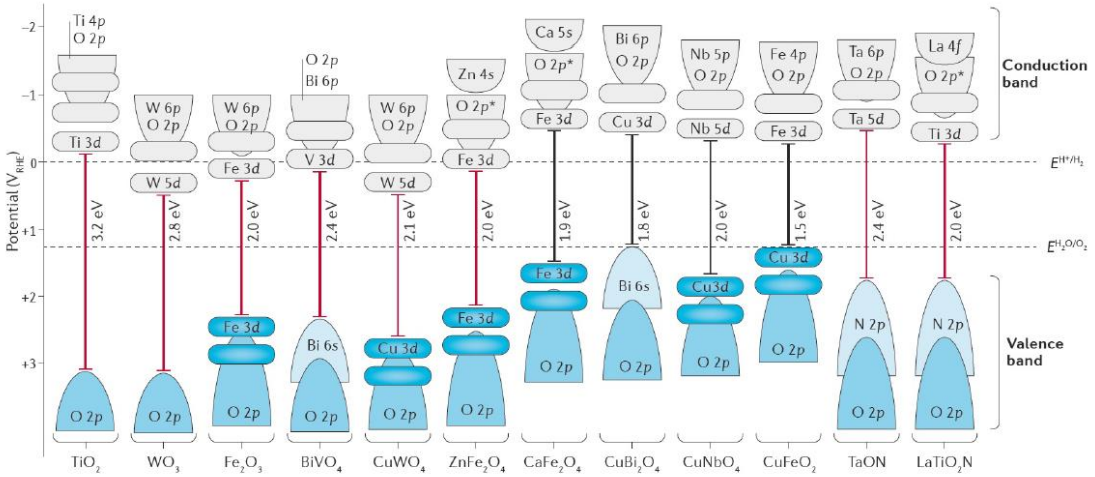

Figure 3. The bandgap edges positons with respect to RHE and the water redox energy levels[19]

1.3.4. Efficient charge transport

The good charge transfer in the semiconductor suppresses the charge recombination, to produce high photoconversion efficiency, and vice versa[18,4].

Many semiconductor systems were utilized for photocatalytic water splitting such as metal oxides, metal sulfides, metal phosphides, metal nitrides, oxynitrides, and selenides. Metal oxides exhibit an extreme chemical and photo-stability. Up to date, TiO_2 has been demonstrated as one of the most used photocatalytic semiconductors for PEC water splitting owing to its low-cost, non-toxicity, high chemical and physical stabilities, and excellent photocatalytic properties[20-21].

1.4. TiO_2 properties as photoelectrode

In addition to its major role in assisting the degradation of organic pollutants[22], and the high efficiency dye-sensitized solar cells[23], TiO_2 exhibits several properties that made it one of the most studied metal oxides due to various structural and electronic properties that will be presented in the following sections:

1.4.1. The structural properties of TiO_2

TiO_2 can be found in several crystalline structures i.e., anatase, rutile[24], and the brookite, which is the least common structure due to the difficulties of its preparation (monoclinic baddeleyite-like form and an orthorhombic are rare phases can exist under high pressures)[25]. The high activity of the anatase TiO_2 and the good stability of the rutile phase motivated the scientists to study them more[26]. The three crystalline structures of TiO_2 are formed by six oxygen atoms surrounding single Ti atom in octahydral configuration (TiO_6) chains, with a noticeable difference in the distortion and assembly pattern between the atoms bonding. The unit cell of each crystalline phase are presented in figure 4.

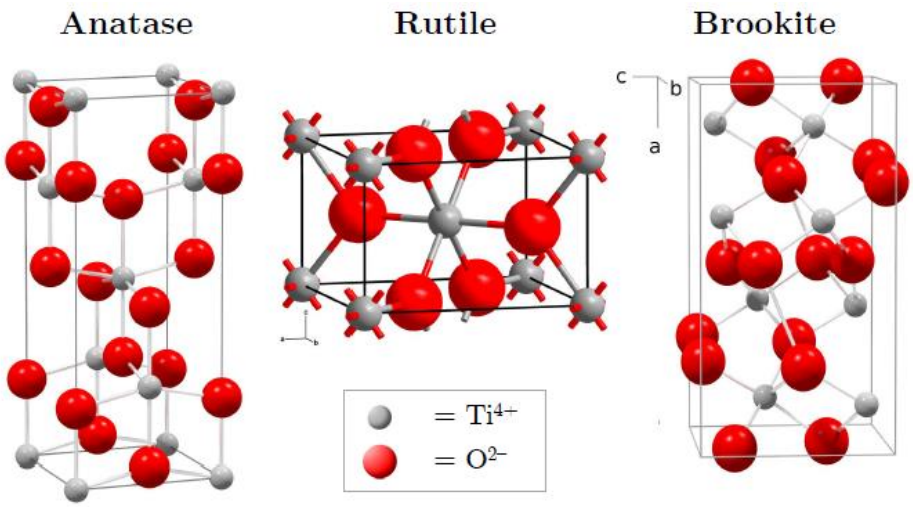

Figure 4. The unit cell of the TiO_2 crystalline phases (the most common)[27]

As it can be seen from Figure 4, the rutile phase exhibits a little orthorhombic distortion, where the anatase phase is showing more significant distortion and lower degree of symmetry compared to the rutile. Furthermore, the Ti-Ti distance of the rutile phase is smaller and the Ti-O distances are larger than the anatase phase. The phase transformation from a phase to another can take place by heating; for example, anatase can be converted to rutile upon heating at 600 °C. The phase transformation is affected by various parameters such as the annealing conditions, grain size, morphology, and the presence of dopants or impurities[28].

1.4.2. The electronic properties of TiO_2

The wide-bandgap of the three phases is different to some extent; the anatase and the bookite phase are indirect transition bandgaps with Eg= 3.2 eV[29] and 3.4 eV[30], respectively. The rutile phase exhibits a direct bandgap equals to 3.05 eV[31]. Figure 5 shows a schematic diagram illustrates the concept of both direct and indirect band gap.

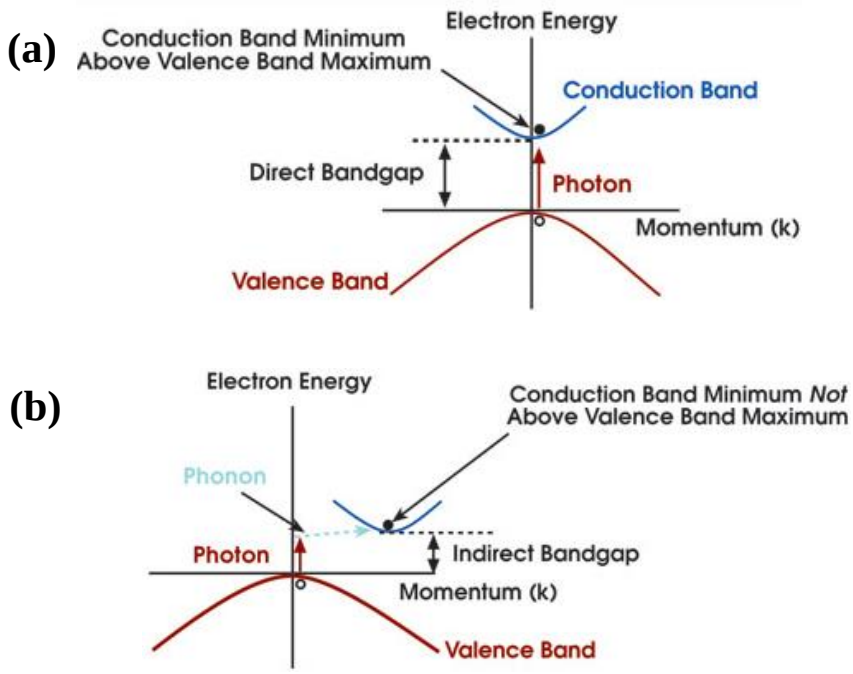

Figure 5. illustration shows the band structure of (a) direct and (b) indirect gap semiconductors

As it is represented in Figure 5a, the direct band gap exhibits conduction band minimum above the valance band maximum exactly occurs at same value of momentum. On the other hand, the indirect bandgap, in Figure 5b, means that the conduction band minima is not above the valance band maxima with different value of momentum[32]. The indirect bandgap causes losing some energy to change the momentum of the photoinduced electrons.

1.5. TiO_2 photocatalyst drawbacks

Despite the several advantages of metal oxides and in particular TiO_2, they (especially TiO_2) exhibit some drawbacks such as; high rate of charges recombination, which limit the photocatalytic activity. The main limitation that can suppress the practical application of a photocatalyst is the low separation possibility of the

photoinduced electron-hole pairs in most of the stable and commonly used forms. Thus, it is required to fabricate a photocatalyst with improved charge separation to afford efficient water splitting[33]. In addition, the wide band gap of ~3.2 eV and of ~3.0 eV for anatase and rutile phases, respectively[34]. Which means that only photons with a wavelength in the ultraviolet (UV) region (λ < 380–400 nm) is absorbed and thus only ~4% of the solar spectrum can be absorbed to promote charge carrier generation in the material. The development of a photocatalyst that can absorb the energy in the visible region is required because the visible light constitutes 43% of the incoming solar energy to the earth.

In order to overcome these limitations, various strategies have been developed such as nanostructured morphology engineering[35], surface modification[36], elemental doping[37] and construction of heterostructure[38].

1.6. TiO_2 photocatalyst performance enhancement approaches

1.6.1. Nanostructure morphologies

The nanostructured design of semiconductor materials attracted the scientists for water splitting. In general, the nanostructures can improve the photocatalytic performance because of the higher surface area of the material which provides more active sites, efficient charge separation, and facilitated charge transfer with shorter route. Several one-dimensional (1D) TiO_2 nanostructures were studied and investigated (like nanrods[39], nanowires[33], nanotubes[40], nanofibers[41], nanosheets[42]…etc.) due to the less recombination of the charge carriers, which is needed for better PEC performance.

1.6.2. Coupling with heterostructures

Semiconductor coupling is approach used to utilize the solar light for water splitting. The heterojunction is considered as a hybrid system that provides synergic

improvement in PEC performance because of the less electron-hole recombination, and the fast separation of the photogenerated species. The coupling of large energy bandgap with a small bandgap semiconductor that has more negative conduction band than the larger bandgap semiconductor can improve the efficiency of PEC water splitting. The conduction band electrons have the ability to be injected from smaller energy bandgap into the larger bandgap semiconductor[43]. Several heterojunction systems of TiO_2 were studied and investigated to overcome the shortage in the photocatalytic activity of TiO_2. Metal sulfides[44], phosphates oxides and metal phosphides[45], and metal nitrides[46] and oxynitrides, were used as heterojunctions materials coupled with TiO_2.

Elemental doping approach can increase carrier concentration and creates dopant energy levels in the energy gap of TiO_2, which effectively narrows the band gap of the material and consequently causes the red-shift of the optical absorption to the visible light regions[47, 48, 49]. However, the main focus of this work is to improve the PEC performance of TiO_2 NRs by the formation of heterostructures.

1.7.Heterojunctions with TiO_2

Although the band edge alignment is a vital factor to improve the photocatalysis performance (will be explained in 1.7.1 section), materials that exhibit a conduction band more negative than the TiO_2 are supposed to be suitable for coupling with it. The combination of certain materials with TiO_2 is expected to form a heterojunction that shows expanded light absorption capability and lower recombination rate of charge carriers. For instance, several oxynitride perovskites semiconducting materials were fabricated for various applications such as solar driven water splitting[50,51]. These novel photocatalysts can absorb most of the visible light due to its bandgap. Metal oxides and oxynitrides are suitable candidates for the

heterojunction with TiO_2. Nonetheless, most of oxides and oxynitrides are narrow bandgap semiconductors which have several drawbacks such as the fast charges recombination rate and the high trapping density[52].

1.7.1. Band alignment in heterojunctions

Semiconductors-semiconductor heterostructures could be classified into three types based on the band alignment of the two semiconductors as shown in Figure 6. The two semiconducting materials (SC-A: semiconductor 1, and SC-B: semiconductor 2) form a heterojunction of type I, type II, or type III. In type I heterojunction, the VB of SC-A is more positive in potential than the valance band of SC-B and the CB of SC-A is more negative than that of SC-B. Type II shows different case where the valance band of SC-A more negative than that of SC-B, and a conduction band situation similar to type I. However, type III exhibits valance band and conduction band lower than the conduction and valance bands of SC-A.

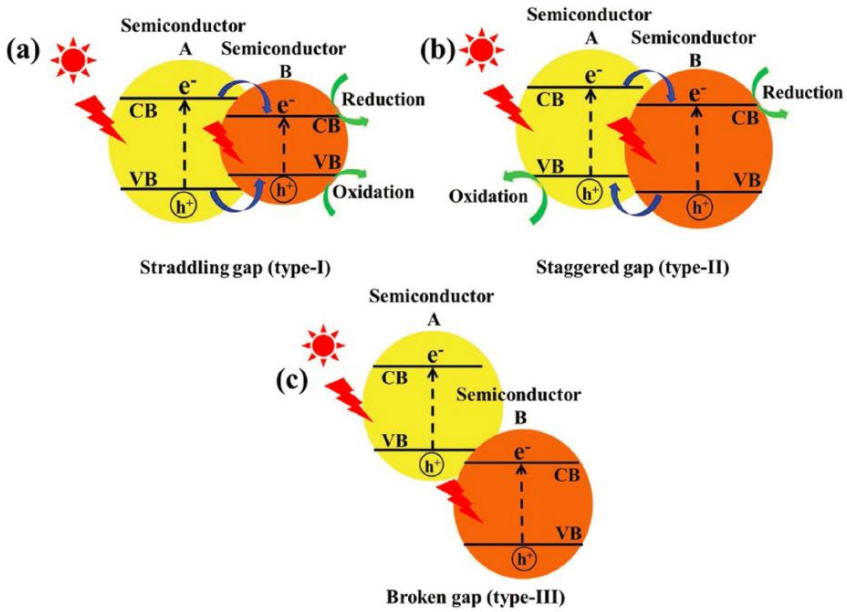

Figure 6. Band diagram that shows the three possible band alignment types: (a) type I (b) type II (c) type III[53]

In type I, the charge carriers will accumulate in SC-B (the smaller bandgap) and this will facilitate the electron-hole recombination and decrease the photocatalytic activity (Figure 6a). Type II exhibits better photocatalytic performance because of the better electron-hole pair separation because they are distributed in both semiconductors of the heterojunction. Electrons move from CB of SC-A to the CB of SC-B to initiate the reduction reaction, and holes move from VB of SC-B to VB of SC-A to facilitate the oxidation reaction (Figure 6b). However, no heterojunction system can be formed in type III alignment because electrons and holes in SC-A or SC-B do not have the ability to transport from one semiconductor to another and the system will be treated as separated as two separated semiconductors materials (Figure 6c)[54].

In this work, the photoelectrochemical performance of TiO_2 will be improved by applying two enhancement strategies to improve its photocatalytic activity. Firstly, by the fabrication of one-dimensional (1D) nanostructured morphology of the TiO_2 nanorods. Secondly, by the coupling with bandgap matched material to form a heterostructure hybrid system. The Nano-dimensions of the TiO_2 rods can provide several advantages because it can provide shorter diffusion length perpendicular to the charge colleting substrate, yielding lower recombination rate of e-h pairs. In addition, a larger surface area for more reaction sites, and excellent light trapping. The rapid charge transfer pathway for the carrier collection is one more advantage for using the nanostructured materials. The usage of another photocatalytic material to form the heterostructure helps in lowering the band gap of the TiO_2 by shifting the absorption edge to the visible region. In addition, it improves charge separation for lower recombination rates, which results in better solar PEC performance for water splitting.

CHAPTER 2: LITRETURE REVIEW

Since the early report on photoelectrochemical activities of titanium dioxide (TiO_2) for hydrogen production from water splitting, which demonstrated by Fujishima and Honda in 1972[55], a variety of semiconducting materials have been investigated for PEC application[56]. Up to date, TiO_2 has been demonstrated as one of the most used photocatalytic materials for PEC water splitting due to its low-cost, non-toxicity, high chemical and physical stabilities, and especially excellent photocatalytic properties[20]. Several 1D TiO_2 nanostructures were studied and investigated (such as nanorods, nanowires, nanotubes, nanofibers…etc.) due to the less recombination of the charge carriers, which is needed for better PEC performance. The nanostructured morphology engineering approach involves creation of specific morphologies with novel properties [36] while the surface modification approach can decrease the surface recombination velocity of the material[57]. Due to the water splitting application that is based on the absorption of sunlight, the growth of TiO_2 is required to be on conductive transparent substrate. The first step was achieved when Bin Liu and Eray S. Aydil were able to grow single-crystal, rutile nanorods of TiO_2 on the fluorine-doped tin oxide (FTO) glass substrate by using simple hydrothermal technique and they were able to provide the experimental details that indicate the parameters that could control the shape, length, diameter, and other different structural properties of the grown film[58]. The controlled growth technique on a transparent conductive substrate opened new horizons for achieving enhanced cell performance for different applications. A variety of parameters could control the growth of the TiO_2 nanorods, the growth time, growth temperature, effect of the substrate, the influence of the reactants' concentrations, the acidity of the medium, the type of the titanium source, and the addition of the surfactants[59].

Several strategies were demonstrated to overcome the shortage of TiO_2 PEC

performance such as elemental doping of metals and nonmetals. Ta doped TiO_2 nanorods showed improved charge separation for the PEC water splitting using the hydrothermal technique on FTO substrate. The location of Ta^{+5} dopant in the TiO_2 crystal lattice caused a reduction in the diameter of surface TiO_2 nanoparticles. Among several studied Ta concentrations, the photocurrent yield was ~1.36 mA cm^{-2} at 1.23 V. The enhancement of the photocurrent was explained by the larger interface area of the surface TiO_2 nanostructure and the effect of Ta doping on the electronic conductivity[60]. Tin (Sn) could be introduced as a TiO_2 photocatalyst's dopant based on inducing sub-band level on the conduction band that enhances the photocatalytic performance of the TiO_2 semiconductor by supporting the separation of the photoexcited charges[61,62]. Er could play a role for doped TiO_2 as a study mentioned the results of lowering the band gap from 3.31 eV to 3.26 eV for the 0.4% Er[63]. However, Fe doped TiO_2 photocatalytic performance was studied and compared to the un-doped TiO_2 semiconductor. It was found that Fe^{+3} dopant provided a stabilization effect to the photocatalyst. The improvement of the photocatalyst performance was introduced based on reducing the band gap energy that results in more absorption in the visible light region (red shift of optical response toward visible light)[64]. Darinka Primc and others published a work mentioned that the active material of the photoanode was prepared using doped TiO_2 with amorphous iron oxide. It was found that the photocurrent was increased to 2.2 mA cm^{-2} at 1.23 V under the illumination of 1.5 AM simulation of sunlight due to the iron doping where the iron oxide heterojunction and the creation of the layer that cause the blocking[65]. Furthermore, co-doping technique can be used to achieve an improved photocatalytic performance of the TiO_2 photocatalyst by using two different dopants[66]. Recently, co-doping of TiO_2 with two elements was used to achieve higher PEC activity. Hwang et al fabricated a Sn and C co-doped TiO_2 nanostructure with 2.8 mA

cm^{-2} at 1.23 V photocatalytic activity[67]. Another group mentioned that W and C co-doped TiO_2 produced a photocurrent density of 1.8 mA cm^{-2} at 1.23 V. The improvement of the performance is originated from the synergistic effects of co-doping technique due to the better electrical conductivity. However, Ni/Si TiO_2 co-doped system showed enhanced photocatalytic activity for water splitting[68]. Another study provided a preparation method for N/Si co-doped TiO_2 system grown on FTO glass substrate which resulted in improved solar to hydrogen efficiency equals to 1.1%[69].

Table 1. List of Several Dopants Types Used for TiO_2 Doping.

Dopant	**Doping type**
Ta	Metal doping
Sn	Metal doping
Er	Metal doping
Fe	Metal doping
Fe_2O_3	Non-metal doping
Sn/C	Co-doping
N/Si	Co-doping

TiO_2 heterojunction method had attracted a lot of attention due to the combination between the photocatalytic of the TiO_2 and the ability to increase the efficiency of it by coupling with another semiconducting material, which can increase the charges transfer and decrease the recombination rate[70]. ZnO@TiO_2 heterostrcture was fabricated and analyzed by a group of scientists. The fast and low cost sol-gel based preparation method allowed the deposition of anatase TiO_2 on ZnO nanowires. The air

annealing effect was studied and it was found that it induces lower charge carrier recombination and enhanced charge separation. The photocurrent was obtained ant it showed 2.2 times improvement in the PEC performance compared to the pristine material[71]. $BiOCl/TiO_2$ photocatalyst was tested as visible light photocatalyst fricated via sol-gel technique. The prepared heterostructure showed higher visible-light-responsive photocatalytic performance than the separated two component of the heterostructure. The degradation rate of the rhodamine B was used to calculate the PEC improvement and it was 46 times higher than the pristine TiO_2 and 11 times higher than the pure BiOCl. The improvement of the photocatalytic performance could be attributed to the higher visible light absorption and the enhanced charge separation efficiency[72]. The photocatalytic activity of TiO_2 was improved by the fabrication of RuO_2/TiO_2 nanobelt heterostructure. The improved catalytic performance was achieved under UV and visible light irradiation due to the better separation of the photogenerated species and the accelerated transport of charges[73,74]. Fe_2O_3-TiO_2 is another attractive heterostructure that showed several times enhanced photocatalytic activity. The heterostructure was synthesized by plasma enhanced-chemical vapor deposition technique. The higher photocurrent enhancement is attributed to the more favorable hole dynamics for water oxidation, and because of the enhancement of the separation of the electron-hole pairs[75]. MoS_2/TiO_2 heterostructure was fabricated for efficient photocatalytic hydrogen evolution process. The high photocatalytic activity was achieved due to the higher conductivity of MoS_2 edge site that can enhance the interfacial conductivity and limit the electron-hole recombination. Furthermore, MoS_2/TiO_2 heterostructure can regulate the electrons transfer after the separation from TiO_2, which facilitates the photoexcited charges to be transferred to the active site on the MoS_2[76,44]. Another TiO_2 heterostructure was synthesized to promote photocatalytic

activity, CdSe/TiO_2 nanotubes heterostructure was created via chemical bath deposition (CBD). The content of CdSe dopants into TiO_2 was studied to determine the optimum content for the improvement of the PEC performance. Furthermore, coupling TiO_2 with CdSe provided better photocurrent density than the pristine CdSe material. The experimental results showed lower average excitation lifetimes, which reveals the participation of the photoexcited CdSe in injecting electrons into TiO_2[77]. Bi_2MoO_6 nanosheet/TiO_2 nanobelt heterostructure was prepared via hydrothermal method. The prepared heterostructure showed an excellent photocatalytic activity and high photocatalytic oxygen production under irradiation of the solar illumination. The improved PEC performance under UV and visible light can be ascribed to the large specific surface area, matched energy band of heterostructure, higher charge transfer efficiency, and lower photoelectron-hole recombination rates[78,79]. CeO_2/TiO_2 heterostructure was reported in the literature as an efficient photocatalyst with several more advantages such as low cost, and recyclability[80]. The simple hydrothermal method allows the assembly of the CeO_2 nanoparticles on the rough surface of the TiO_2 nanobelts. Both UV and visible photocatalytic activity of the CeO_2/TiO_2 heterostructure was greatly improved compared to the pure TiO_2 and pristine CeO_2 material[81]. Graphene oxide (GO) was assembled on the top of TiO_2 nanobelt to form a heterostructure via an in situ photochemical reduction facile method. This method was conducted by wrapping TiO_2 nanobelts with reduced graphene oxide nanosheets. This heterostructure improve the separation of the photoinduced charge carriers due to the zero bandgap of graphene and the presence of Ti-O-C bonds, which produces higher photocurrent performance and enhanced photocatalytic activity. This remarkably better photocatalytic performance is because of the special and unique electronic properties of the reduced graphene oxide. GO/TiO_2 heterostructure showed improved

photocatalytic activity for water splitting that produces hydrogen. Furthermore, it exhibits a good stability after five cycles because no loss of activity was achieved, with an excellent recyclability property[82]. Fe_2TiO_5-TiO_2 nanocages heterostructure was synthesized to achieve highly efficient solar energy conversion by using heterostructured semiconductor photocatalyst. The heterostructure photocatalyst was fabricated to achieve enhanced PEC performance for water splitting and stable heterostructure formation. It was observed that the heterojunction and the well-defined hollow structures are needed to improve the performance of the semiconductor photocatalyst to be used as an efficient photocatalyst[83].

Metal oxides with perovskite structure are essential functional materials that are used in many applications such as superconductors, gas sensors, and photocatalysts[84,85]. A group of scientists fabricated a heterostructured composite of $BiVO_4/TiO_2$ via hydrothermal technique. The coupling between TiO_2 and $BiOV_4$ helps in the enhancement of the photocatalytic activity for the heterojunction system and in getting better charge separation. The photocurrent experimental results showed a noticeable improvement in the photocatalytic activity with higher current density compared to the pristine TiO_2 and $BiVO_4$ materials under visible light illumination. The heterojunction formation facilitated the charge separation of the photogenerated species, which was proved by the smallest arc of the Nyquist plot of the electrochemical impedance spectroscopy (EIS)[86]. Another novel heterostructure was $BiOF/TiO_2$, which was prepared by solid-state stirring. The optimum molar ratio of the heterojunction system (1:3) showed seven times higher photocurrent density than BiOF nanopowder and two times higher than TiO_2. The noticeable photocatalytic enhancement was explained by the red shift of the absorption edge of TiO_2 from the UV to visible region of the spectra that allows lowering the bandgap and absorption more visible light. In addition, the

BiOF improved the charge separation process[87]. Another interesting heterostructure is hydrogenated TiO_2/ZnO nanorods on FTO substrate via solution-coating method. The proposed preparation method allowed achieving homogenous distribution of ZnO coating on the TiO_2. The remarkable PEC water splitting and the red shift is due to the hydrogenation process that creates oxygen vacancies in the TiO_2 and interstitial hydrogen in ZnO, which produced several times higher current density than the pure TiO_2 and ZnO[88]. However, three times higher current density than TiO_2 was obtained using $ZnIn_2S_4/TiO_2$ nanorod heterojunction by using the hydrothermal technique for water splitting application. Furthermore, the system showed a high cycle stability, and the onset potential was reduced from +0.05 to -0.5. The improved and fast electron-hole transfer and separation was verified by the EIS measurements of the interface charge transfer kinetics[89,90]. CdS/TiO_2 nanotubes were synthesized by ac electrodeposition to enhance the photoelectrode performance toward the water splitting. The fabricated heterostructure exhibited much better photocurrent density in the visible wavelengths than the pristine TiO_2. Furthermore, the time and the voltage of the ac deposition affect directly the architecture of the heterostructure, which is related to the photocatalytic performance of the electrode and improves the water photocleavage due to the more contact area of the electrode and the electrolyte[91]. A variety of approaches can be used to achieve the red shift toward the visible region light absorption, $CoTiO_3$ –encapsulated TiO_2 heterostructure was fabricated to enhance the TiO_2 nanowires photoresponse to the visible light range. The encapsulation of $CoTiO_3$ on the surface of TiO_2 nanowires allows the formation of core-shell heterostructure. In comparison with the pure TiO_2, the photocatalytic activity of the heterostructure was improved about 30% more, and the charge carrier concentration was increased 346% than the pristine material[92]. Oxynitrides had been studied as effective photcatalysts due to their bandgap

that allow the absorbance of visible light. $LaNbON_2$ was studied as a solar photocatalyst for water oxidation purpose. The unique band gap of the material of 1.65 eV allows to absorb the light at around 750 nm at wide visible-light absorption band. It was found that under the irradiation of light on $LaNbON_2$, water oxidation takes place due to the anion vacancies that act as donors in semiconductors[93]. $BaTaO_2N$ was introduced as a promising photoanode for water splitting by annealing in argon environment. The charge separation and the crystallinity from the surface to bulk showed an improved solar driven water splitting process[94]. Therefore, it is promising to study the coupling of oxynitride material with TiO_2 to obtain enhanced PEC performance.

CHAPTER 3: EXPERIMENTAL

3.1. Materials

Titanium (IV) butoxide $C_{16}H_{36}O_4Ti$ (97%) was purchased from Sigma Aldrich, USA. Hydrochloric acid HCl (37%) Analar NORMAPUR was purchased from VWR Chemicals, UK. Lanthanum (III) nitrate hexahydrate $La(NO_3)_3 \cdot 6H_2O$ (99.99%), Ammonium molybdate $(NH_4)_6Mo_7O_{24} \cdot 4H_2O$ (99.98%) and citric acid ($C_6H_8O_7$) had been bought from Sigma Aldrich, USA. The FTO substrates were bought from Ossila Company, UK. Deionized water (DI) was the solvent in this study. All materials were used as received without any treatment.

3.2. Material Preparation

Hydrothermal synthesis technique has attracted much attention for fabricating nanostructures that have unique properties for wide range of applications. The substances crystallize in high temperature and pressure in presence of solvent in a closed system. The technique produces highly pure and homogenous crystal structures with novel properties by allowing the size control of the product in shorter times compared to the other techniques. The hydrothermal reaction is performed in a steel vessel (autoclave) that the synthesis conditions are controlled by the temperature, and/or the pressure. Usually, the internal removable part of the autoclave is made of Teflon.

3.2.1. Synthesis of TiO_2 nanorods

The fabrication of TiO_2 nanorods was conducted using hydrothermal method by preparing 30 mL aqueous hydrochloric acid (HCl) freshly prepared solution through adding 15 mL concentrated HCl (Sigma Aldrich, Analytical grade, 37%) to 15 mL deionized (DI) water obtained directly from water deionizer (Millipore, Direct-Q 5UV). After magnetically stirring for 10 minutes, the addition of 0.3 mL Titanium (IV)

butoxide (TiBu, Sigma Aldrich, 97%) took place and gently stirred for 15 min. Subsequently, the prepared solution was placed into a 100 mL Teflon-lined stainless steel autoclave (BAOSHISHAN, PTFE Lined Vessel), where the cleaned FTO substrates (1.5 x 2 cm) arranged inside the Teflon beaker with a FTO side facing the Teflon beaker wall. Figure 7 demonstrates the Teflon-lined stainless steel autoclave that was used for the hydrothermal synthesis. Prior to the hydrothermal synthesis, the FTOs were cleaned by ultrasonication in acetone, methanol, and DI water separately for 10 min each, respectively. The hydrothermal growth was carried out at 180 °C for 10 hours in an electric oven (Nabertherm, Model: TR-061RN) and allowed to cool down to room temperature. The fabricated TiO_2 on the FTO/glass were rinsed extensively with DI water several times and dried on air. The preparation method was reported in the literature before [95]. Lastly, the annealing step was conducted.

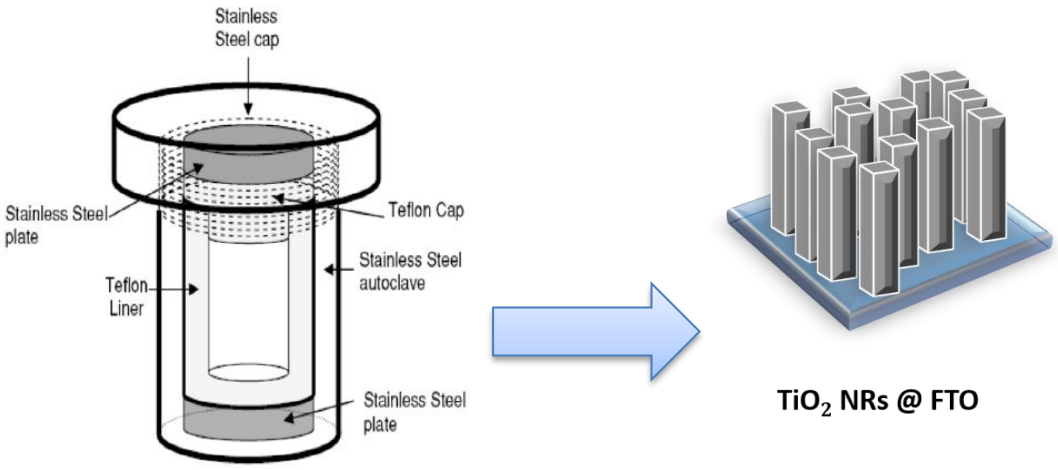

Figure 7. Illustration of Teflon-lined stainless steel autoclave

3.2.2. Thermal treatment

The annealing treatment is used to convert the physical properties of the materials. The as-fabricated TiO_2 was annealed for crystallization and for increasing the electrical conductivity. The thermal treatment was conducted in air at 400 °C for 4 hours with heating ramp of 1degree/minute, and the cooling down at room temperature. MTI GSL 1500X-OTF 2 inches tube furnace was used for the thermal treatment process.

3.2.3. Preparation of $LaMo(ON)_x$

$LaMoO_9$ was synthesized by using sol-gel method[96] with 0.2 g $La(NO_3)_3 \cdot 6H_2O$, 1.2 g $(NH_4)_6Mo_7O_{24} \cdot 4H_2O$ and 0.8 g of citric acid to achieve the metal molybdates. The 30 mL prepared solution of $La(NO_3)_3 \cdot 6H_2O$, $(NH_4)_6Mo_7O_{24} \cdot 4H_2O$ and citric acid was refluxed by heating the water bath to 90 °C and stirring for 3 hours until the observation of the transparent sol. Then, after the drying of the gel for 5 h at 100 °C, the sol was mixed with the gel. Next, the calcination step of dried gel powder for 4 h at 600 °C in air at heating rate of 5 degree/minute (°C /min) to obtain the $LaMoO_9$ powder. To achieve the oxynitride of the product, additional annealing step in ammonia was conducted at 700 °C for 2h and by heating ramp of 5 °C /min.

3.2.4. Preparation of $LaMo(ON)_x/TiO_2$ heterostrostructure

The electrophoretic deposition technique (illustrated in Figure 8) was used to fabricate the heterostructured hybrid system of TiO_2. A 50 mL beaker was used to place 0.0025 g of $LaMo(ON)_x$ and it will be ultrasonicated in 30 mL acetone for 20 min. The 0.1 g iodine will be added to the sonicated suspension and sonicated again for 5 min in ultrasonic bath at room temperature. Then, the two probes of the DC power supply was connected to the FTO as blank (negative side) and the as-fabricated TiO_2 to the positive side of the power supply, and both will be immersed directly on the prepared iodine

suspension. The direct current (DC) electric field of 15 V will be applied for 5 min. All the experiments were prepared by the same deposition conditions and conducted at the room temperature.

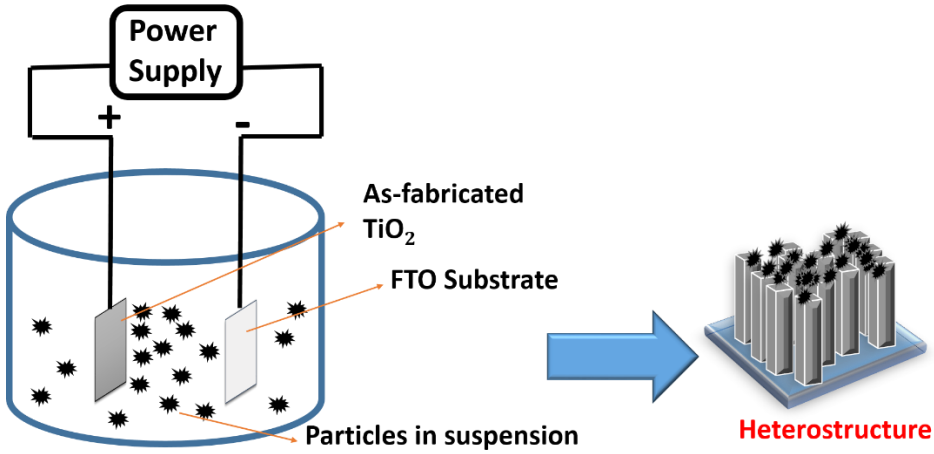

Figure 8. Illustration of the electrophoretic deposition preparation process

3.3. Photoelectrochemical measurements

The generated photocurrent is recognized as a measure to evaluate the photoelectrodes performance for water splitting using the current-voltage measurements. This type of measurements provide detailed information about[97]:

1. Energy conversion efficiency, photocurrent density and the dark current of the photoelectrode as a function of potential.
2. The photocurrent sign and onset potential.
3. The electron-hole recombination rate and the transport limitations.

Quartz three-electrode system (Figure 9) is used to measure the photocatalytic performance toward the water splitting via potentiostat. The three-electrode system consists of a working electrode, which is used at specific potential versus the reference electrode, and the obtained current by changing the applied voltage under light illumination or in the dark is recorded. This permits the construction of current-voltage

plot. However, the performance of the counter electrode will not be relevant due to the role of potentiostat in supplying whatever voltage between the counter electrode and the photoelectrode (working electrode) to maintain the current at a definite voltage with respect to the reference electrode.

Impedance is the measure of the circuit's ability to resist the flow of electrical current. The term impedance refers to the frequency dependent resistance to current flow of a circuit element and it can be represented by either Nyqist plot or Bode plot. The electrochemical cells can be modeled as a network of passive electrical circuit elements called equivalent circuit, which can be calculated (double layer capacitance, electron transfer resistance, electrolyte resistance…etc.) and compared to the experimental EIS response of the cell[98].

Instrumentation

The PEC measurements were performed by using Potentionstat/Galvanostat INTERFACE 1010 from GAMRY INSTRUMENTS, USA. The standard three-electrode system was connected to the working electrode to the studied sample, and the platinum (Pt) wire was connected to the counter electrode and Ag/AgCl standard electrode was the reference electrode by carrying out the PEC measurements in a quartz electrochemical cell (PINE). The measurements were conducted in non-buffered 1M KOH solution (electrolyte). The copper crocodile clipper was used to hold the sample and to establish the electrical connection by being in contact with the uncovered portion of the FTO substrate. The light source SunLite ^{TM} from ABET TECHNOLOGIES, USA, model: 11002 was the solar simulator. The quartz photocell was placed in 1 sun equivalent distance, as the power intensity was kept at 100mW/cm^2 which was calibrated by silicon reference cell (ABET). The illumination of light was by 100 Watt Xenon Arc Lamp. The PEC performance was investigated by conducting three

experiments: linear sweep voltammetry (LSV), electrochemical impedance spectroscopy (EIS), and chronoamperometry. The linear sweep voltammetry was carried out under light and on dark with initial voltage of 0.4 to 1.5 V vs Ag/AgCl at 5 mV s^{-1} scan rate and step size of 1mV/s. The electrochemical impedance spectroscopy experiments were conducted under light and on dark from initial frequency of 10^5 Hz to final frequency of 10^{-2} Hz at DC voltage of 0.8 V, and by collecting 10 points/decade. In addition, the chronoamperometry experiment at voltage of 0.8 V for 200 seconds by alternating the light on/off each 10 seconds.

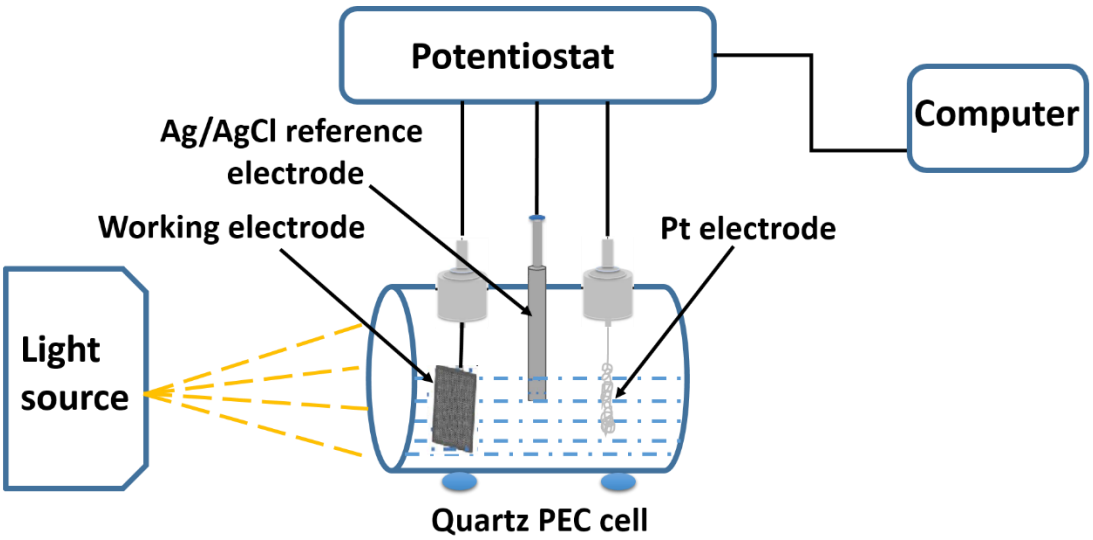

Figure 9. Illustration of quartz three-electrode system of PEC measurements

3.4. Material characterization and Equipment

The fabricated materials have been characterized to study the structural, morphological, and photoelectrochemical properties by using several characterization techniques.

3.4.1. Scanning electron microscope (SEM)

The scanning electron microscope (SEM) is used to study surface morphology

of the sample by focusing the high-energy electron beam (0.2-30 KeV) on the scanning probe that scan the specimen surface. The primary electron beam will interact with the sample and produces several responses (illustrated in Figure 10) that can be measured using different detectors and produce various information about the studied sample.

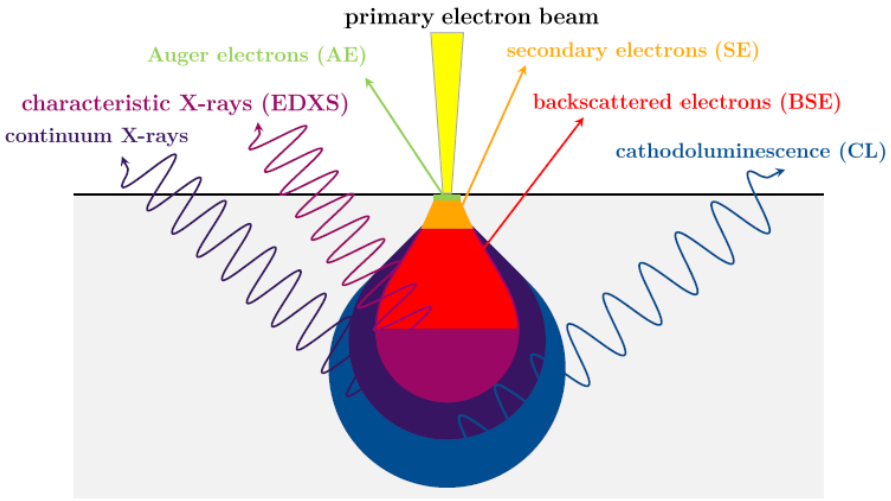

Figure 10. Schematic diagram of the interactions between the sample surface and the primary electron beam[27]

The incident primary electron beam interacts with the studied sample and produces back-scattered electrons (BSE), secondary electrons (SE), and X-rays. The elastic scattering between the primary electrons and the nuclei is the reason behind the BSE interaction. The BSE provides a qualitative information about the composition since the specimen with higher atomic number produces more BSE. However, the inelastic interactions with the sample generates SE when the amount of transferred energy is enough. Various signals can be produced due to the interaction with the specimen such as X-rays that can identify the elements by the characteristic X-rays for each element, Auger electrons, and catholuminescence[99].

Instrumentation

The morphology of the TiO_2@FTO/Glass and the heterostructures was observed by SEM (FEI NOVA NANOSEM 450) operated at acceleration voltages between 0.5 and 30 kV. The SEM is equipped with energy dispersive spectroscopy (EDS) operating at primary beam acceleration voltage between 10-20 kV.

3.4.2. Raman spectroscopy

Using a laser beam source, the inelastic scattering of the monochromatic light happens because of the excitation of the vibration modes in atoms of the sample. As a result of the inelastic scattering, the energy of the re-emitted photons from the sample will be measured and recorded. However, the re-emitted photons energy can be shifted up or down the original monochromatic light frequency (Raman effect)[100]. The shift provides information about the rotation and vibration transitions in the sample. The obtained Raman spectrum is a relation between the scattered light intensity and the Raman shift. The Raman shift is a change in wavenumbers between the laser light source (W_L frequency) and the scattered radiation of the sample. Figure 11 illustrates the possible scattering types of Raman spectroscopy. The obtained Raman spectra consists of Stokes spectral lines (with frequencies lower than W_L) because the Stokes spectral lines have higher intensities than the anti-Stokes scattering does (spectral region with higher frequencies than W_L). The scattered light that preserves its wavelength is the Rayleigh scattering[101].

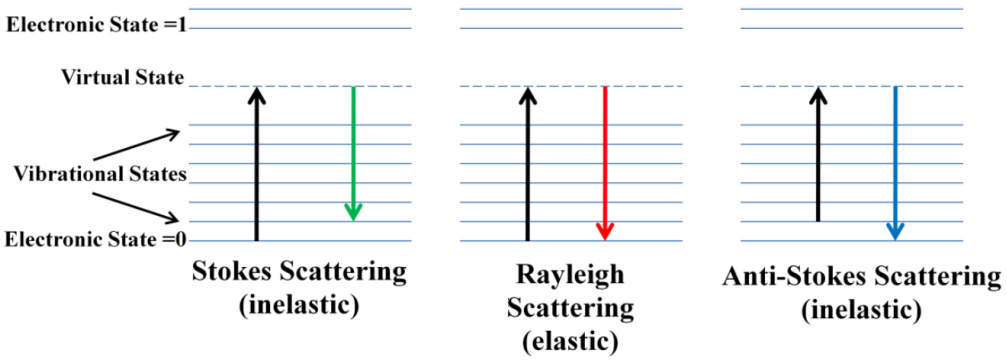

Figure 11. A schematic diagram shows the scattering types of Raman spectroscopy[102]

Instrumentation

A ThermoFisher Scientific Raman spectrometer equipped with a microscope MPlan 10X/0.25 BD was used to obtain the Raman spectra of TiO_2 and the heterostructures. The samples were excited with laser beam of 633 nm wavelength before spectra recording.

1.4.3. X-Ray diffraction

The non-destructive analysis technique is used to recognize the structural properties and the various phases in the characterized material. The crystalline planes of the material will diffract the incident X-rays to form destructive or constructive interference. Based on Bragg's law, the constructive interference occurs when the path length difference of the scattered x-rays of the crystal planes is an integer multiple of the incident wavelength (Bragg's law)[103]:

$$n\lambda = 2d_{hkl} \sin \theta_{hkl}$$

θ_{hkl} describes the angle between the three crystal planes and the incident X-rays, and d_{hkl} is referred to the distance between the crystal planes of Miller indexes (*hkl*) (Figure 12). Which indicates that the diffracted X-rays detector should be located at an angle $2\theta_{hkl}$ with respect to the incident X-rays[104].

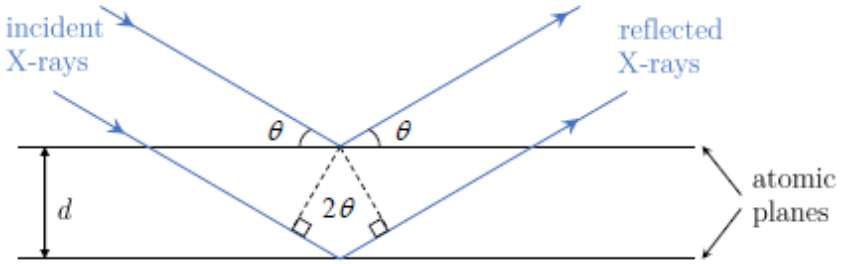

Figure 12. Schematic view of Bragg's law

Instrumentation

PANalytical EMPYREAN X-Ray diffraction,40 KV/30 mA, Cu-Kα radiation (λ = 1.54056 Å) was used to obtain the θ-2θ spectra at a scan rate of 2°/min with a diffraction angle 2θ between 10° and 80°. The system is equipped with a detector that allows data collection from -45° to +45° vertically and from 0° to 160° horizontally.

1.4.4. X-ray photoelectron spectroscopy (XPS)

X-ray photoelectron spectroscopy (XPS) is a unique analysis technique that provides an information about the surface (2-5 nm depth) composition. The quantitative elemental and chemical analysis is used to detect the elemental structure of the surface by exciting the core shell electrons via X-rays capable to break the binding energy (B.E) between the electron and the nucleus of the atom which will produce a kinetic energy of the electron that will be calculated through a sensitive detector (electron energy analyzer) that can calculate the kinetic energy (K.E.) which is characteristic for each element. Consequently, the bonding nature, and the oxidation status will be detected. Figure 13 demonstrates the main parts of the XPS instrument including electron gun, electron analyzer, focused X-ray beam, and monochromator[105].

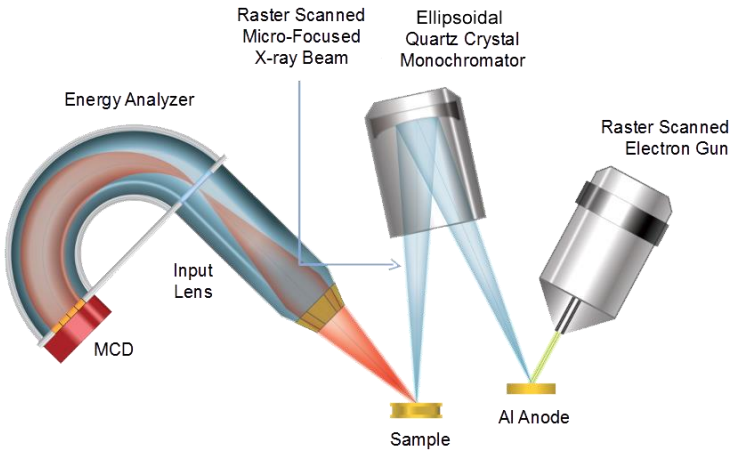

Figure 13. A schematic diagram of the XPS instrument[106]

The x-rays focused beam with 1.5 kV will be directed to the sample where the photo-emitted electrons with energy lower than 1.5 kV will be ejected from the sample's surface of the specimen. Then, the electron collection lens will direct the escaped electrons toward the electron energy analyzer that measures the kinetic electron of the electrons and the electrons detector counts the number of electrons that indicates the intensity of the obtained spectra. However, XPS technique requires ultra-high vacuum inside the chamber (less than 10^{-8} Torr)[107].

Instrumentation

The measurements were conducted using X-ray photoelectron spectroscopy (AXIS Ultra DLD) which designed with monochromatic Al- Kα electrons source and with spherical mirror electron analyzer that detect the surface electrons and count its kinetic energy and its number.

1.4.5. UV-Vis spectroscopy

Ultraviolet-visible spectroscopy is a nondestructive technique that is used to determine the optical transitions of the material. This optical characterization method allows monitoring the electronic transitions of the semiconductors. The spectrometer

measures the transmittance and reflectance of the sample, which allows to calculate the absorbance of the opaque material, and to approximate the bandgap of the material by using Tauc relation[108]. The sample would be placed in the holder in a direction of the light beam to study the interaction between the light and the deposited material. For the transmittance measurements, the sample should be placed in the entering light side to the integrated sphere. However, for the reflectance measurements, the sample should be placed on the other side of the sphere (as illustrated in the following illustration).

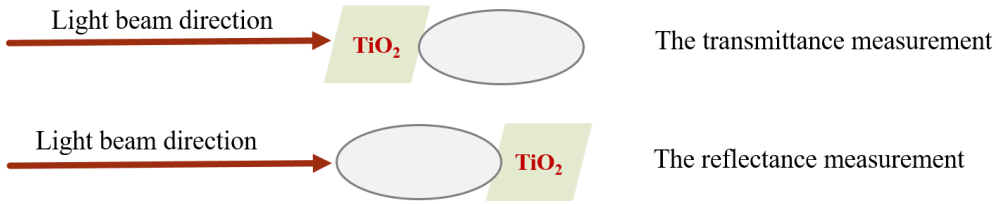

Figure 14. UV-Vis experimental setup of the transmittance and the reflectance measurements

However, the blank (FTO) transmittance values should be subtracted from the sample transmittance measurements to eliminate the interference of the glass.

Instrumentation

The UV-Vis spectroscopy was performed with a Perkin Elmer Lambda 1050 spectrophotometer equipped with 150 mm diameter integrated sphere (reflectance larger than 99% in 400-1500 nm range). The optical characterization measurements were conducted between 250-800 nm wavelength.

CHAPTER 4: RESULTS AND DISCUSSION

4.1. Fabrication of TiO_2 nanorods

TiO_2 nanorods were synthesized via hydrothermal technique using several preparation conditions such as growth temperature, growth time, and HCl/Ti source volume ratio. The nanorods growth was conducted onto fluorine-doped tin oxide (FTO) substrates based on previously reported method[58], followed by thermal treatment (annealing) step at 400 °C for 4 h in air. The three parameters were studied to identify the optimized growth conditions that will affect the NRs shape, morphology, and the PEC performance of the prepared TiO_2. The prepared TiO_2 NRs samples were examined by morphological and photoelectrochemical studies. SEM was used to investigate the morphology, TiO_2 nanorods density, orientation, and the length. In addition, PEC measurements were conducted to evaluate the activity of different samples and to determine the optimized conditions that provide the highest PEC performance.

4.1.1. The effect of growth temperature

TiO_2 NRs were prepared at three different temperatures (140,160,180 °C) to investigate the influence of growth temperature on the morphology and PEC performance. Other growth parameters are held constant i.e. (the growth time is 10 hours and the HCl:Ti volume ratio is 50:1). Figure 15 a, b, c shows the top view SEM images of the prepared TiO_2 at different growth temperatures. It is observed that the temperature has remarkable effect on the shape and density of fabricated NRs. As the temperature increased from 140 °C to 180 °C, the average diameter of the NRs increased from about 50 nm for the sample prepared at 140 °C to 100 nm for the sample prepared at 160 °C. TiO_2 NRs sample prepared at 180 °C showed average diameter close to 1 μm, and the NRs shape changed from circular to rectangular shape.

Furthermore, the cross–sectional SEM images (Figure 15 d, e, f) show that the length of the TiO_2 nanorods increases with increasing the growth temperature. The NRs lengths were found to be 1.2 μm, 3.2 μm, 5 μm for 140 °C, 160 °C, and 180 °C, respectively. It is also noteworthy that the density of NRs increases with increasing the growth temperature.

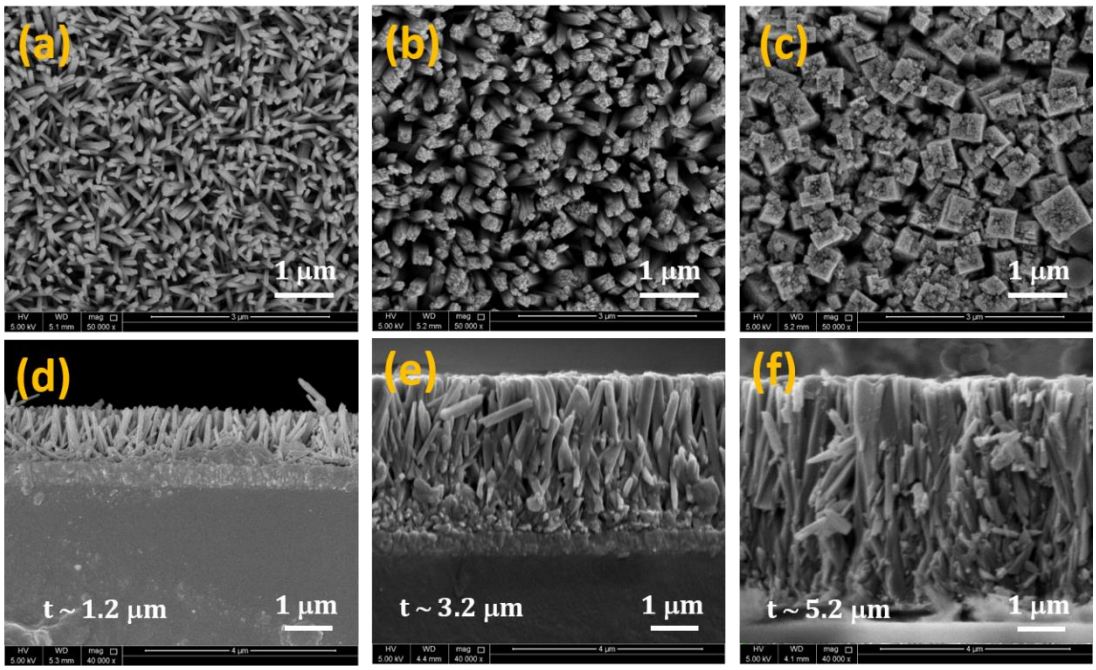

Figure 15. Top-view SEM images of TiO_2 NRs fabricated at: (a) 140 °C (b) 160 °C (c) 180 °C and cross-sectional SEM images of TiO_2 NRs fabricated at: (d) 140 °C (e) 160 °C (f) 180 °C

The PEC performance of TiO_2 prepared at different temperatures is given in Figure 16. Figure 16a represents the linear sweep voltamograms (LSV) of TiO_2 samples measured in 1 M KOH solution at 25 °C. It shows that the onset voltage (E_{onset}) is 1.1 V for 140 °C, 0.85 V for 160 °C, and almost 1.4 V for 180 °C. These results confirm that the sample prepared at 160 °C revealed the highest catalytic activity. The photoelectrochemical performance of samples was further confirmed by

electrochemical impedance spectroscopy (EIS). Figure 16b exhibited Nyquist plots of samples prepared at different temperatures in 1 M KOH solution. The results depicted that the radius of semicircular arc decreases in the following order: 140 °C (2425 Ω cm^2) > 180 °C (2150 Ω cm^2) > 160 °C (312 Ω cm^2). This confirms that the sample prepared at 160 °C has the lowest resistance and thus the highest PEC activity. This can be verified by the chronoamperometric measurement at 0.8 V vs. Ag/AgCl (Figure 16c). Sample prepared at 160 °C exhibits the highest photocurrent density (1.68 mA/cm^2). As a result, the growth temperature of 160 °C is selected to be optimum growth temperature due to the morphological and PEC experimental results. The obtained PEC experimental data are summarized in Table 2.

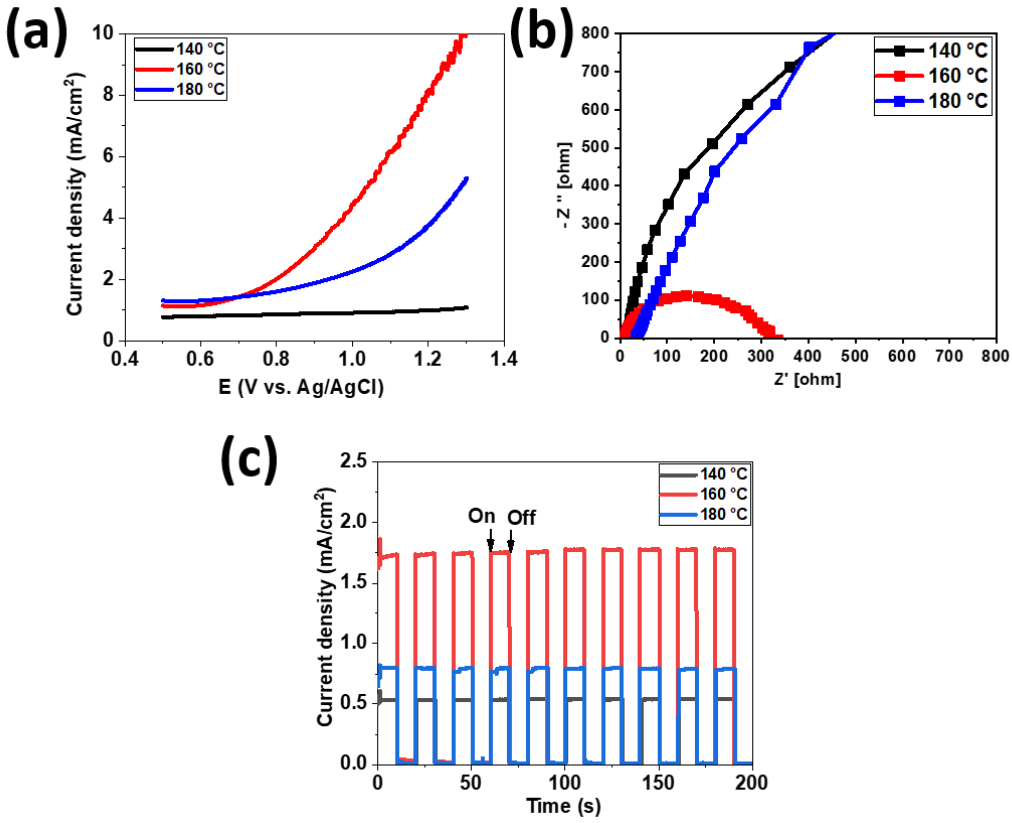

Figure 16. PEC measurements of TiO_2 fabricated at 140 °C, 160°C, and 180 °C: (a) Linear sweep voltammograms under light (b) Nyquist impedance plots of different-

electrodes recorded at 0.8 V vs. Ag/AgCl in 1 M KOH. (c) Amperometric on-off curve at 0.8 V vs Ag/AgCl with light on/off cycles

Table 2. Summary of PEC Experimental Results for the Effect of Temperture.

Growth temperature (°C)	**E_{onset} potential (V vs. Ag/AgCl)**	**R_p (Ω cm^2)**	**Maximum current density (mA cm^{-2})**
140	1.10	2425	0.52 mA/cm^2
160	**0.85**	**312.40**	**1.68 mA/cm^2**
180	≈ 1.4	2150	0.77 mA/cm^2

4.1.2. The effect of growth time

Upon optimization of the growth temperature at 160 °C, the effect of growth time on the morphology and PEC activity was investigated. TiO_2 NRs were prepared at different growth periods i.e. 6, 10, 14 h at 160 °C and HCl:Ti volume ratio of 50:1. Figure 17 represents top view and cross-sectional images of the prepared samples. It is evident that the increase in the growth time led to increasing of the length of the NRs. The average measured length of TiO_2 NRs was found to be 2.5 μm, 3.2 μm, and 3.7 μm for growth times of 6, 10, and 14 h, respectively (Figure 17 d, e, f).

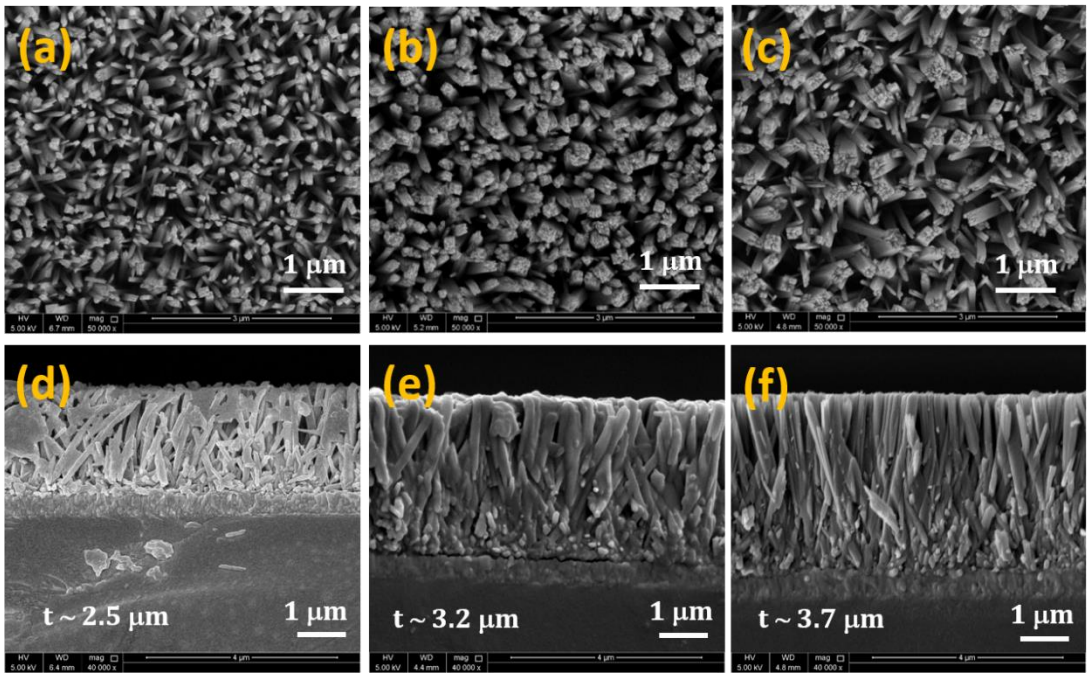

Figure 17. Top-view SEM images of TiO_2 NRs prepared at different growth period : (a) 6 h (b) 10 h (c) 14 h and cross-sectional SEM images of TiO_2 NRs prepared at different growth period: (d) 6 h (e) 10 h (f) 14 h

The PEC performance of samples was investigated by electrochemical measurements. Figure 18a depicts the linear sweep voltammograms of TiO_2 NRs prepared a different growth times in 1 M KOH solution. The results show that the sample prepared in 10 h has the highest PEC activity and lowest onset potential (E_{onset}). Nyquist plots (Figure 18b) showed that TiO_2 NRs prepared in 10 h has the lowest charge transfer resistance. In addition, light on-off chronoamperometric measurements at 0.8 V vs. Ag/AgCl (Figure 18c) revealed current density following the order: TiO_2 NRs-10 h (1.68 mA/cm^2) > TiO_2 NRs-14 h (1.62 mA/cm^2) > TiO_2 NRs-6 h (1.60 mA/cm^2). The obtained PEC experimental data are summarized in Table 3.

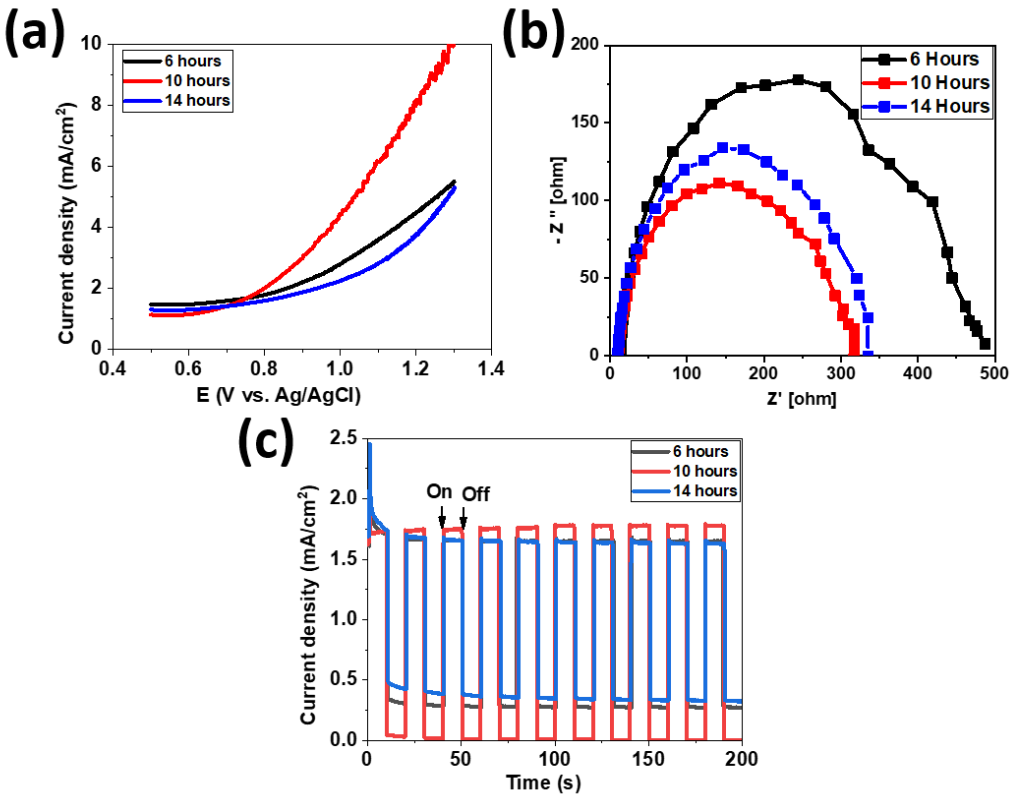

Figure 18. PEC measurements of TiO_2 fabricated at 6h, 10h, and 14h: (a) Linear sweep voltammograms under light (b) Nyquist impedance plots of different electrodes recorded at 0.8 V vs. Ag/AgCl in 1 M KOH. (c) Amperometric on-off curve at 0.8 V vs Ag/AgCl with light on/off cycles

Table 3. Summary of PEC Experimental Results for the Effect of Time.

Growth time (h)	**E_{onset} potential (V vs. Ag/AgCl)**	**R_p (Ω cm^2)**	**Maximum current density (mA cm^{-2})**
6	0.87	324.20	1.60
10	**0.85**	**312.40**	**1.68**
14	0.88	487.30	1.62

4.1.3. The effect of HCl:Ti volume ratio

The effect of HCl:Ti volume ratio factor was studied by changing the HCl:Ti ratio from 40:1 to 60:1 at constant growth temperature (160 °C) and growth time (10 h). Figure 19 shows the top view and cross-sectional SEM images of TiO_2 NRs prepared at different HCl:Ti precursor ratios.

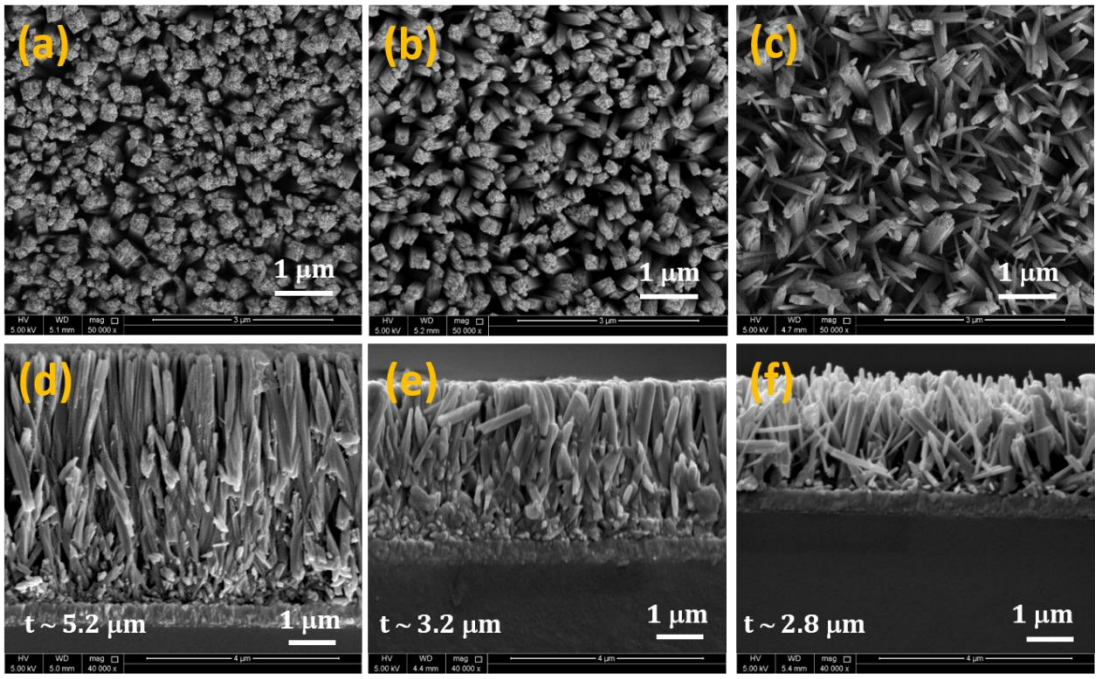

Figure 19. Top-view SEM images of TiO_2 NRs prepared at different HCl: Ti volume ratios : (a) 40:1 (b) 50:1 (c) 60:1 and cross-sectional SEM images of TiO_2 NRs prepared at different growth period: (d) 40:1 (e) 50:1 (f) 60:1

It can be observed that with increasing the ratio of HCl:Ti, the length of TiO_2 NRs decreases. However, the 60:1 sample showed a nonhomogeneous distribution and growth orientation of the NRs. The length of NRs decreased from 5.2 μm in case of (HCl:Ti: 40:1) to 3.2 μm (HCl:Ti : 50:1) to 2.8 μm when the ratio increased to 60:1.

The PEC performance of TiO_2 prepared by using different HCl:Ti volume ratios is given in Figure 20. It represents the linear sweep voltamograms of TiO_2 samples

measured in 1 M KOH solution at 25 °C. It shows that the E_{onset} is 1.05 V for HCl:Ti: 40:1, 0.85 V for HCl:Ti: 50:1, and almost 1.35 V for HCl:Ti: 60:1. These results confirm that the sample prepared at HCl:Ti: 50:1 provided the highest catalytic activity. The photoelectrochemical performance of samples was further confirmed by electrochemical impedance spectroscopy (EIS). Figure 20b exhibited Nyquist plots of samples prepared at different temperatures in 1 M KOH solution. The results revealed that the radius of semicircular arc decreases in the following order: HCl:Ti: 60:1 (≈ 7000 Ω cm^2) > HCl:Ti: 40:1 (≈ 5000 Ω cm^2) > HCl:Ti: 50:1 (312 Ω cm^2). This confirms that the sample prepared by using HCl:Ti: 50:1 has the lowest resistance and thus the highest PEC activity. This can be verified by the chronoamperometric measurement at 0.8 V vs. Ag/AgCl (Figure 20c). Sample prepared by using HCl:Ti: 50:1 exhibits the highest photocurrent density (1.68 mA/cm^2). However, the samples of HCl:Ti: 40:1 and HCl:Ti: 60:1 show photocurrent density 1.39 mA/cm^2 and 0.27 mA/cm^2, respectively. The obtained PEC experimental data are summarized in Table 4.

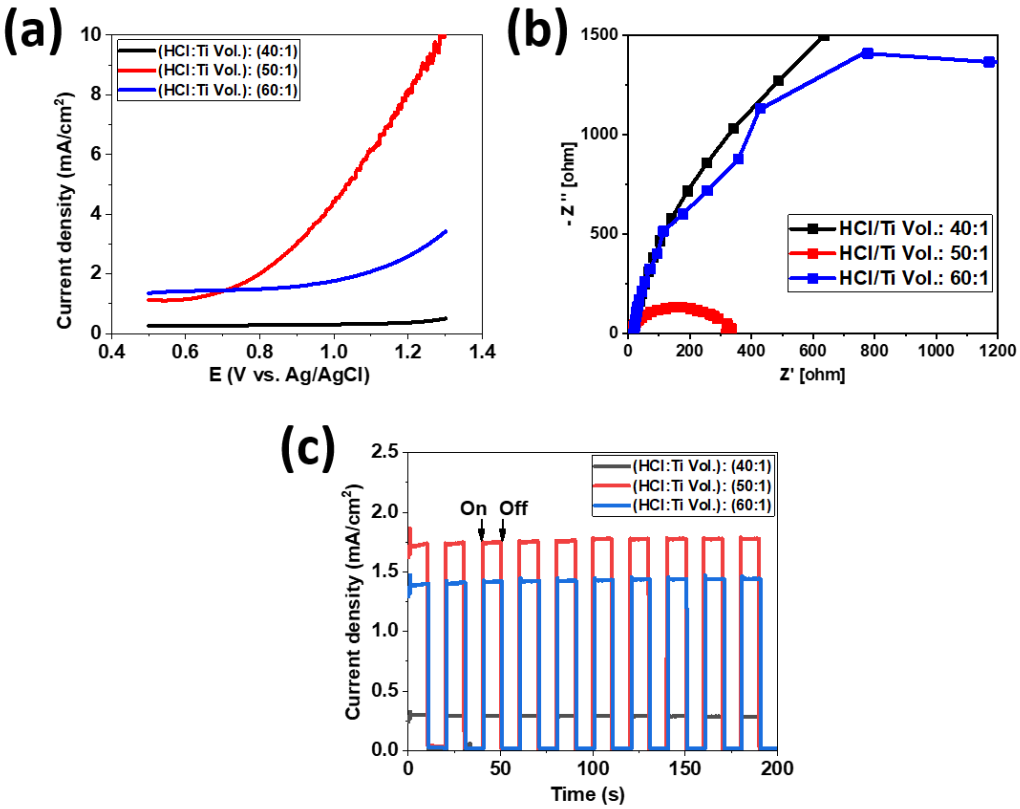

Figure 20. PEC measurements of TiO_2 fabricated using HCl:Ti volume ratios: 40:1, 50:1, and 60:1: (a) Linear sweep voltammograms under light (b) Nyquist impedance plots of different electrodes recorded at 0.8 V vs. Ag/AgCl in 1 M KOH (c) Amperometric on-off curve at 0.8 V vs Ag/AgCl with light on/off cycles

Table 4. Summary of PEC Experimental Results for Effect of the HCl:Ti Volume: Ratio.

HCl:Ti Vol. ratio	E_{onset} potential (V vs. Ag/AgCl)	R_p (Ω cm^2)	Maximum current density (mA cm^{-2})
40:1	1.05	≈ 5000	1.39
50:1	**0.85**	**312.40**	**1.68**
60:1	≈ 1.35	≈ 7000	0.27

To summarize, we investigated the morphology and PEC activity of TiO_2 NRs prepared by varying the growth temperature, growth time, and HCl:Ti volume ratio. The optimized conditions are given in Table 5.

Table 5. Optimized Synthesis Conditions of TiO_2 NRs.

Growth temperature	**160 °C**
Growth time	**10 hours**
HCl:Ti volume ratio	**50:1**

4.2. Characterization of pristine TiO_2

Several characterization techniques were used to determine the characteristic properties of the fabricated TiO_2 to provide structural evidences of the prepared TiO_2 material. The morphology and composition of the pristine TiO_2 NRs were studied by SEM-EDX. The selected optimized sample was grown hydrothermally at growth temperature of 160 °C, growth time 10 hours, and HCl:Ti ratio 50:1. The fabricated samples were thermally treated by annealing on air environment at 400 °C for 4 hours and heating rate 1 degree/min. Figure 21 shows SEM morphology images of the grown TiO_2 NRs on FTO substrates and the EDX spectra of the NRs.

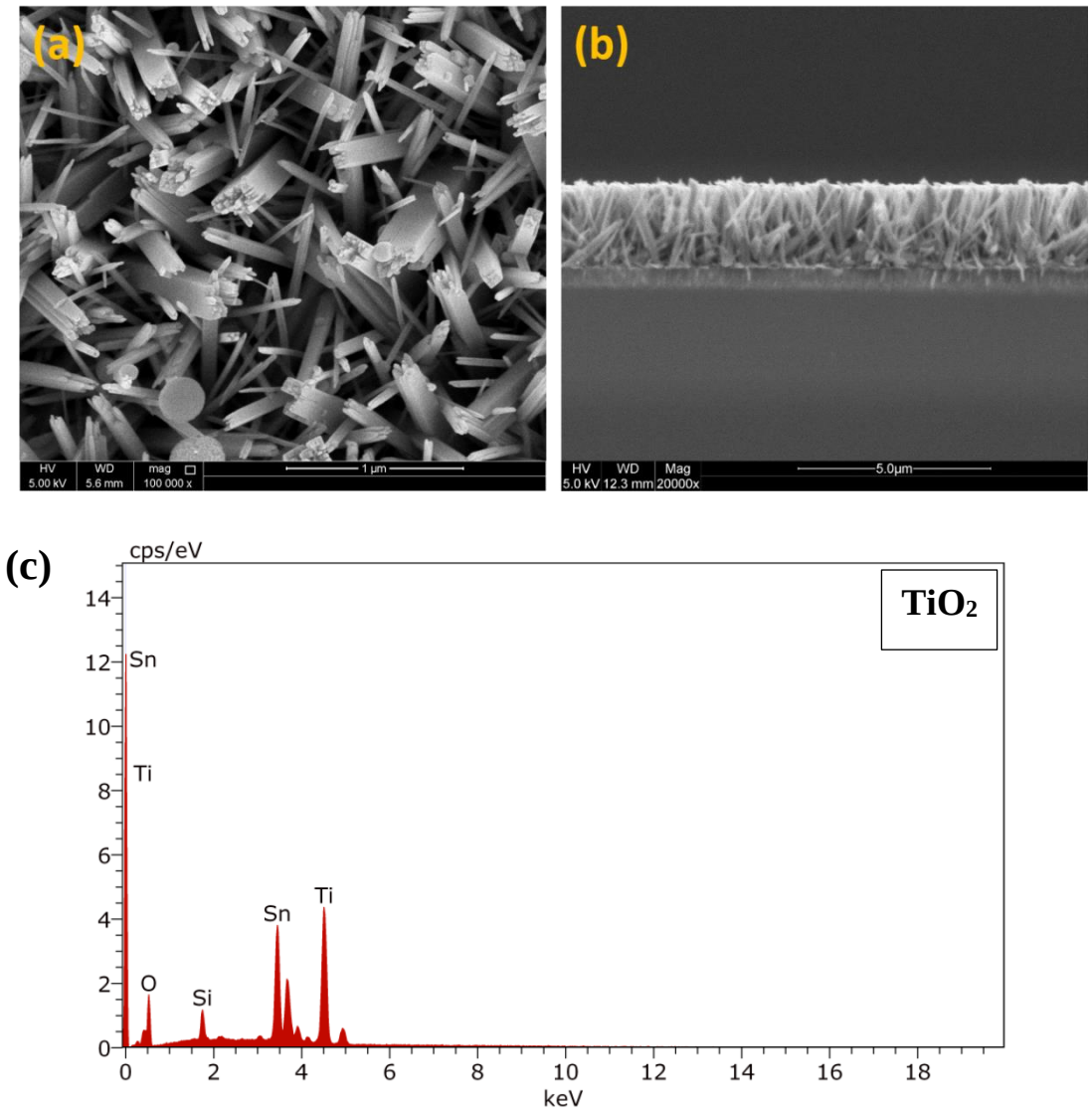

Figure 21. SEM images of the annealed TiO_2 NRs: (a) top view, (b) cross-sectional, (c) SEM-EDX spectrum of the annealed TiO_2

As it can be observed in Figure 21a, the TiO_2 NRs have tetragonal shape and square top facets. The nanostructure forms a uniform coating over the FTO substrate with high adhesion. The NRs growth was (quasi aligned) on the substrate and with an angle for many NRs. Furthermore, it can revealed the tips of the NRs are rougher than the side faces of the NRs owing to the axial growth on the FTO. The cross-sectional SEM micrographs (Figure 21b) revealed the direct contact between the formed NRs and the charge-collecting FTO layer and the well alignment to the FTO substrate. The

formed NRs arrays exhibit a homogenous diameter size distribution of the single NRs over the specimen with a thickness (length of the NR) of approximately 3 μm and average diameter of about 50 nm, the diameter size distribution is between 40 nm and 60 nm. The energy dispersive X-ray spectroscopy (EDX) analysis of the pristine TiO_2 (Figure 21c) shows mainly Ti, O, Sn, and Si elements, which indicate the phase purity of TiO_2 NRs, the Sn and Si are shown due to the FTO/glass substrate.

The crystallinity of pure TiO_2 NRs was investigated using XRD. The diffraction patterns are given in Figure 22. The spectrum of TiO_2 NRs shows the characteristic peaks of the rutile phase for the TiO_2: (101), (211), (002), in addition to diffraction peaks from FTO substrate at 2θ of 37.7°, 41.2°, 51.4°, and 61.6°. The dominant crystalline plane is (101) as revealed by the X-ray diffractogram.

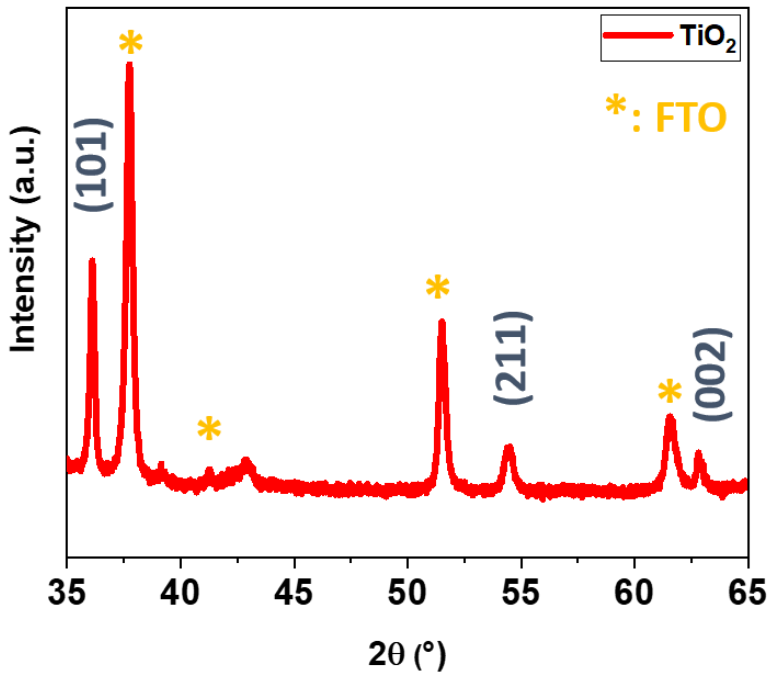

Figure 22. XRD pattern of the as-fabricated rutile TiO_2

The crystallites size was calculated using Scherrer's Equation[109]:

$$D = \frac{K\lambda}{\beta \cos \theta}$$

Where,

D= crystallite size (nm)

K= Scherrer constant (0.9)

λ = Wavelength of the X-ray radiation source (0.15406 nm)

β= The full width at half-maximum of the diffraction peak (FWHM) in radians

θ= Peak positin (radians)

The crystallite size was estimated using the main peaks of the rutile TiO_2: (101) and (002) diffraction peaks. The calculated crystallite size of TiO_2 was found to be 24.9 nm, which is similar to previously reported values[110].

Hydrothermally-grown TiO_2 NRs arrays show a rutile phase structure, which is in accordance with a previously published work[95]. The diffraction peaks at angle of 36°, and 63° are indexed to the crystal planes of (101), and (002) of the rutile phase, respectively. It could be noticed that some diffraction peaks of the rutile TiO_2 are absent such as (110) and (111).

Raman spectroscopy is performed to analyze phase evolution and structure change. It is usually used for structural identification characterizing the different phases of TiO_2 nanostructures, to distinguish a single-phase formation. Raman spectroscopy technique is sensitive to metal-oxide vibrations (metal-oxygen bond) structural environment and the bond length. Figure 23 represents Raman spectra of the pristine rutile TiO_2.

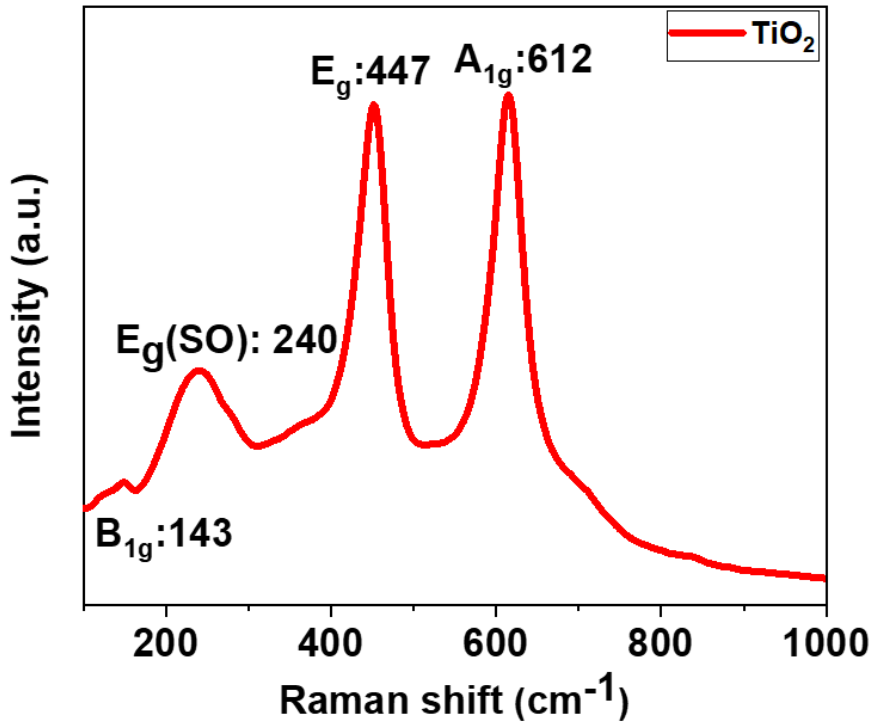

Figure 23. Raman spectra of the pristine rutile TiO_2

As shown in Figure 23, TiO_2 is Raman active in 100-900 cm^{-1} range[111,112]. The rutile TiO_2 has two molecules in the unit cell with the space group $D_{4h}(P4_2/mnm)$ with tetragonal crystal structure[113], and possesses four Raman active modes (B_{1g}, E_g(SO), E_g, A_{1g}) that correspond to the characteristic Raman modes of the rutile TiO_2 structure (rutile phase implies 15 vibrational modes)[114].The E_g mode is associated with the symmetric stretching vibration. The B_{1g} is related to the symmetric bending vibration, and the A_{1g} mode associated with the anti-symmetric bending vibration of O-Ti-O[115]. The E_g band at 240 cm^{-1} is a characteristic multiphonon peak of the rutile TiO_2 phase[116]. However, the intensity of these vibrational modes are correlated with the metal oxide crystallinity, which can be altered by the thermal treatment[117]. The Raman frequencies values are B_{1g}: 143 cm^{-1}, E_g (SO): 240 cm^{-1}, E_g: 447 cm^{-1}, A_{1g}: 612 cm^{-1}, are compared

to the Raman spectra that was recorded by Porto[118] and it showed good agreement.

XPS is a powerful technique to probe the chemical environment of the structure and the surface defects, due to the high sensitivity of this tool to the surface. XPS survey and high-resolution spectra of TiO_2 NRs are presented in Figure 24. The survey spectra showed in Figure 24a revealed the presence of Ti 2p and O 1s peaks of TiO_2, confirming the presence of TiO_2. High-resolution XPS spectra (Figure 24b) shows two peaks assigned to Ti $2p_{1/2}$ and Ti $2p_{3/2}$ spin-orbital splitting photoelectrons are located at binding energies of 464.5 and 458.6 eV, respectively. These peaks are attributed to the crystalline rutile TiO_2. As shown in Figure 24b, the separation between the Ti $2p_{1/2}$ and Ti $2p_{3/2}$ peaks is about 5.91 eV, which is in agreement with previously reported results[119]. The binding energies of Ti 2p having spin-energy separation of 5.91 eV are the characteristic feature of Ti^{+4} in the rutile phase. The difference of 70.1 eV between the binding energy peak of Ti 2p1/2 and O 1s is confirmed previously in the literature, too[107]. Figure 24c represents the high-resolution spectrum of O 1s core level. It depicted the presence of two peaks. The first peak at 529.8 eV can be assigned to O atoms bonded to Ti (Ti-O), while the other peak at 533 eV can be indexed to Ti-OH bonds.

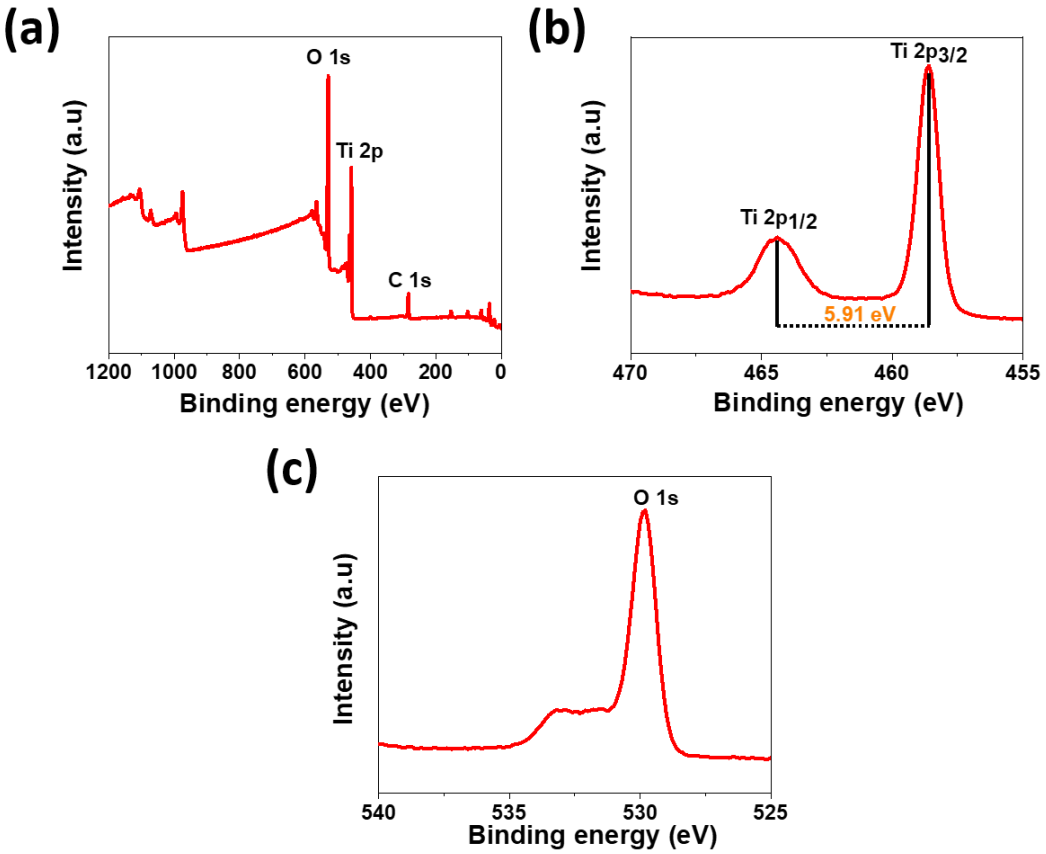

Figure 24. XPS spectra of pristine TiO_2: (a) XPS survey spectra, high-resolution XPS spectra of (b) Ti 2p and (c) of O 1s

Another characterization technique was used to confirm the formation of the TiO_2 NRs using UV-Vis absorption spectra to test the light-harvesting capability of the pristine TiO_2 NRs. Optical absorption spectra was obtained by measuring the transmission and reflection of the film using bare FTO glass as a reference (FTO contribution was subtracted). As illustrated in Figure 25, the absorption edge is positioned at around 410 nm, which is in agreement with the tabulated rutile TiO_2 bandgap of 3.06 eV. TiO_2 can absorb up to 410 nm as shown in Figure 25 due to the wide bandgap. Tauc plot was plotted based on Tauc equation assuming direct allowed transition[120]:

$$(\alpha h\nu)^{1/n} = C\,(h\nu - E_g)$$

The straight line showed in Figure 25 inset represents plot of $(\alpha h\nu)^2$ versus energy ($h\nu$) for TiO_2 (the extrapolation of the abscissa from the linear fit of the curve), through which the band gap was estimated at about 3.06 eV, which is in a good agreement with the reported values in the literature[121].

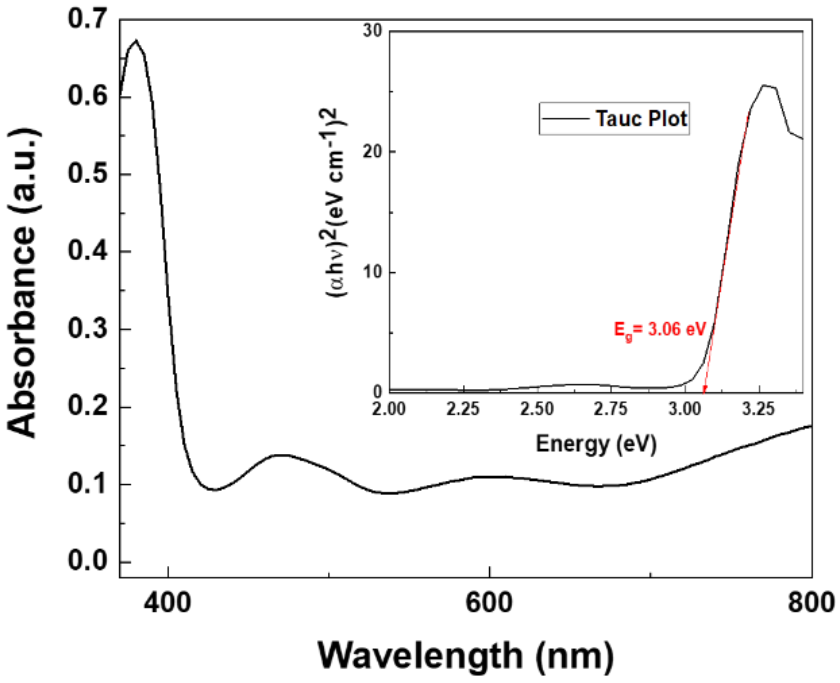

Figure 25. The UV-Vis absorbance spectrum of TiO_2. The inset shows the plot of $(Ah\nu)^2$ versus energy ($h\nu$) for TiO_2

4.3. Heterostructure fabrication

The formation of heterojunction is regarded as one of the devoted approaches to enhance the PEC catalytic performance of TiO_2. Several types of materials have been coupled to TiO_2 (such as sulphides, oxides, nitrides,...etc.). Among them, oxynitrides received great interest owing to their narrow band gap and high photoelectrochemical stability. Herein, we synthesized novel mixed oxynitride $LaMo(ON)_x$ and we coupled it to TiO_2 NRs to enhance their PEC activity.

$LaMo(ON)_x/TiO_2$ heterostructure was synthesized via two-step procedure. In the first step, TiO_2 nanorods (NRs) were prepared using hydrothermal synthesis. After that, $LaMo(ON)_x$ was deposited on the as-fabricated TiO_2 NRs by electrophoretic deposition technique.

4.4. Characterization of the $LaMo(ON)_x$/ TiO_2 heterostructure

The morphology and microstructural details of as-fabricated TiO_2 NRs, $LaMo(ON)_x$, and the $LaMo(ON)_x/TiO_2$ NRs were investigated by SEM. Figure 26a shows SEM image of the as-fabricated TiO_2 with NRs width of 50 nm. Figure 26b reveals the morphology of the $LaMo(ON)_x$ particles obtained by sol-gel method followed by annealing in NH_3. The size of the $LaMo(ON)_x$ particles is around 300-500 nm. $LaMo(ON)_x$/ TiO_2 heterostructure is presented in Figure 26c. The top view SEM image shows an irregular covering of the $LaMo(ON)_x$ on the top of the TiO_2 NRs. The rough surface of the TiO_2 NRs provides a preferential nucleation sites for the $LaMo(ON)_x$ particles to deposit. This results in homogenous coverage of the $LaMo(ON)_x$ on the TiO_2 NRs. The larger irregular–shaped aggregates covering some NRs tips are observed, too. The SEM-EDX spectrum of the heterorstructure (Figure 26d) reveals that the nanorods are composed of Ti and O element (Sn, Si are existed because of the FTO/glass substrate), and the heterostructure is composed of Ti, O, La, Mo, and N.

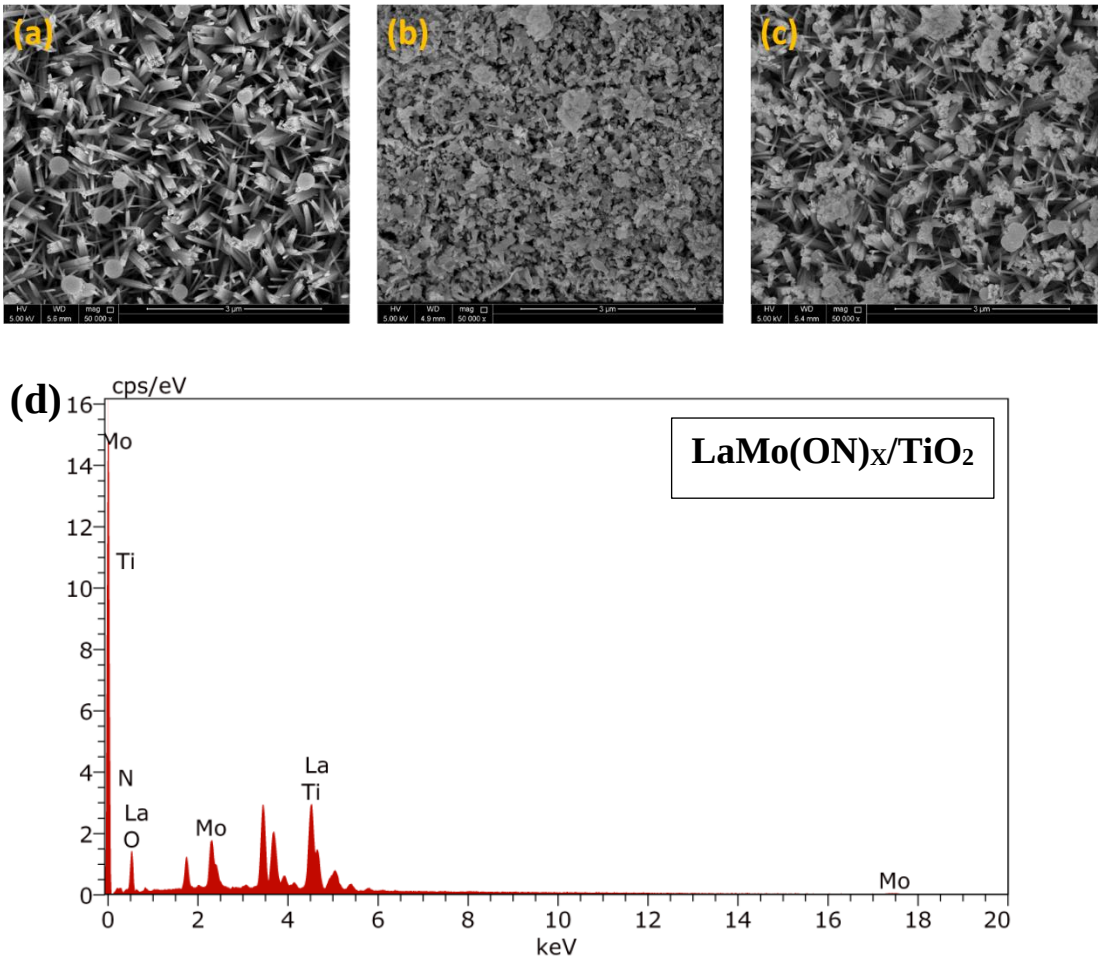

Figure 26. The SEM top view images of (a) pristine TiO_2, (b) $LaMo(ON)_X$, (c) $LaMo(ON)_X$/ TiO_2 (D) SEM-EDX spectrum of $LaMo(ON)_x/TiO_2$ heterostructure

Figure 27 revealed the diffraction pattern of FTO/TiO_2 and FTO/TiO_2/ $LaMo(ON)_x$. The formation of the heterostructure can be confirmed from the XRD spectrum that shows the characteristic peaks of the rutile phase TiO_2 in addition to the $LaMo(ON)_X$ peaks that are located at 15.6°, 22.1°, 27.8°, 39.5°,45.1°,48.8°.

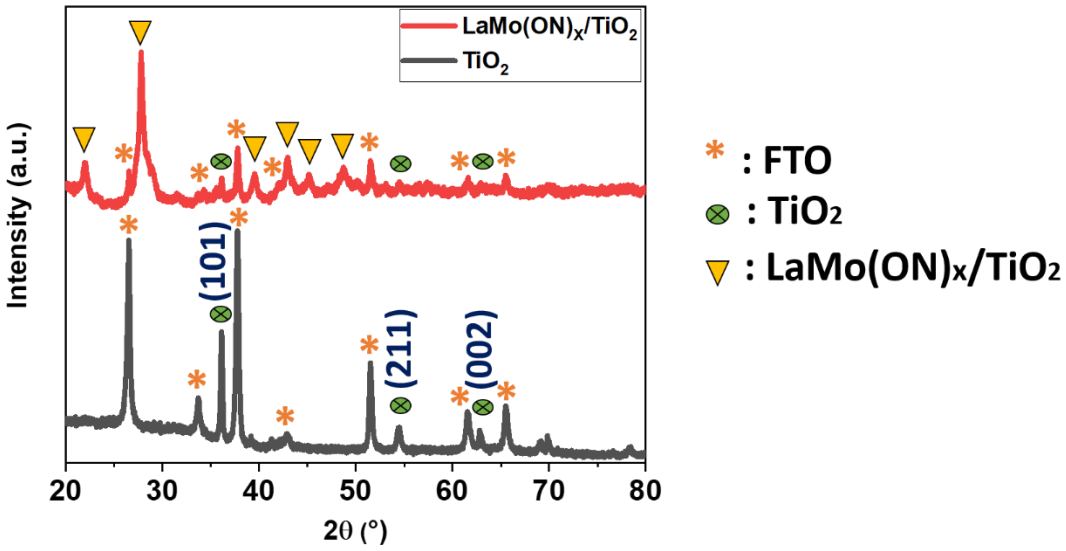

Figure 27. XRD patterns of pure TiO_2 and $LaMo(ON)_x/TiO_2$ heterostructure

Figure 28 demonstrates the Raman spectra of the TiO_2 and $LaMo(ON)_x/TiO_2$. The four rutile TiO_2 characteristic Raman active peaks are observed with typical bands of the rutile TiO_2. However, two additional peaks are observed at around 329.7 cm^{-1}, and 901.5 cm^{-1} for the $LaMo(ON)_x$/ TiO_2 Raman spectra , which can be well-ascribed to the $LaMo(ON)_x$ phase. Furthermore, peaks located at 447 cm^{-1} and 612 cm^{-1} of the heterostructure spectra were shifted to a lower wavenumber of 442.7 cm^{-1} and 609.7 cm^{-1} for E_g and A_{1g} peaks, respectively. The Raman peaks shift toward the lift at 447 and 612 cm^{-1} bands implies an increase in the length of O-Ti-O bonds, which could be explained by the formation of the heterostructure.

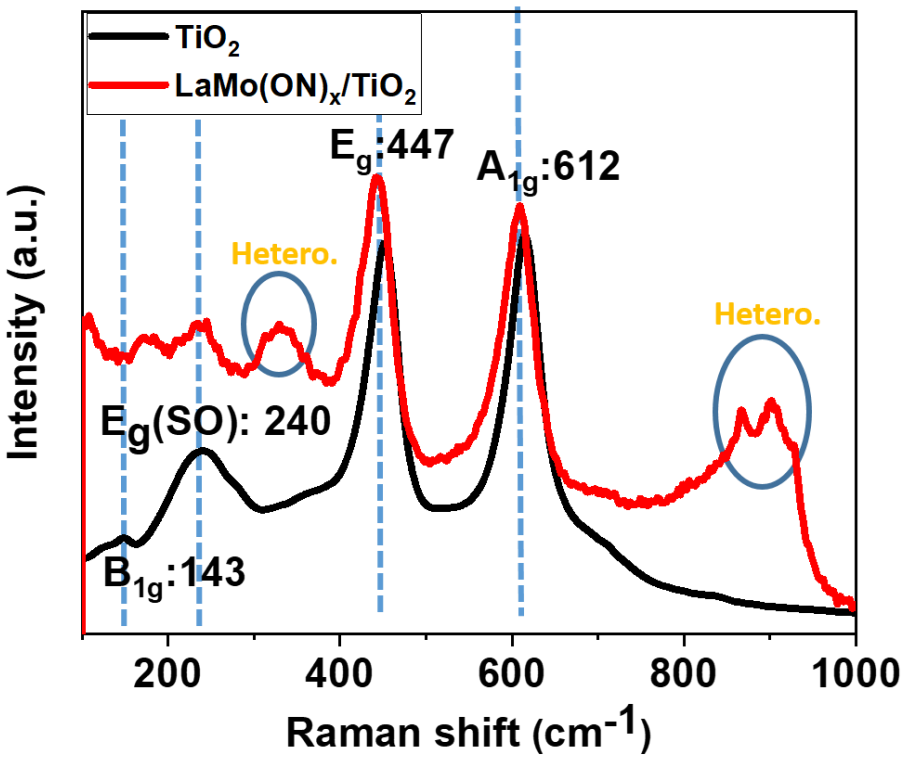

Figure 28. Raman spectra of pristine TiO_2 (black) and $LaMo(ON)_x/TiO_2$ (red)

Figure 29 shows the XPS spectra of the $LaMo(ON)_x/TiO_2$ heterostructure. The survey spectrum demonstrates the existence of the elemental La, Mo, N, O, and Ti components as presented in (Figure 29.a), which confirms the phase purity of the $LaMo(ON)_x/TiO_2$ heterostructure.

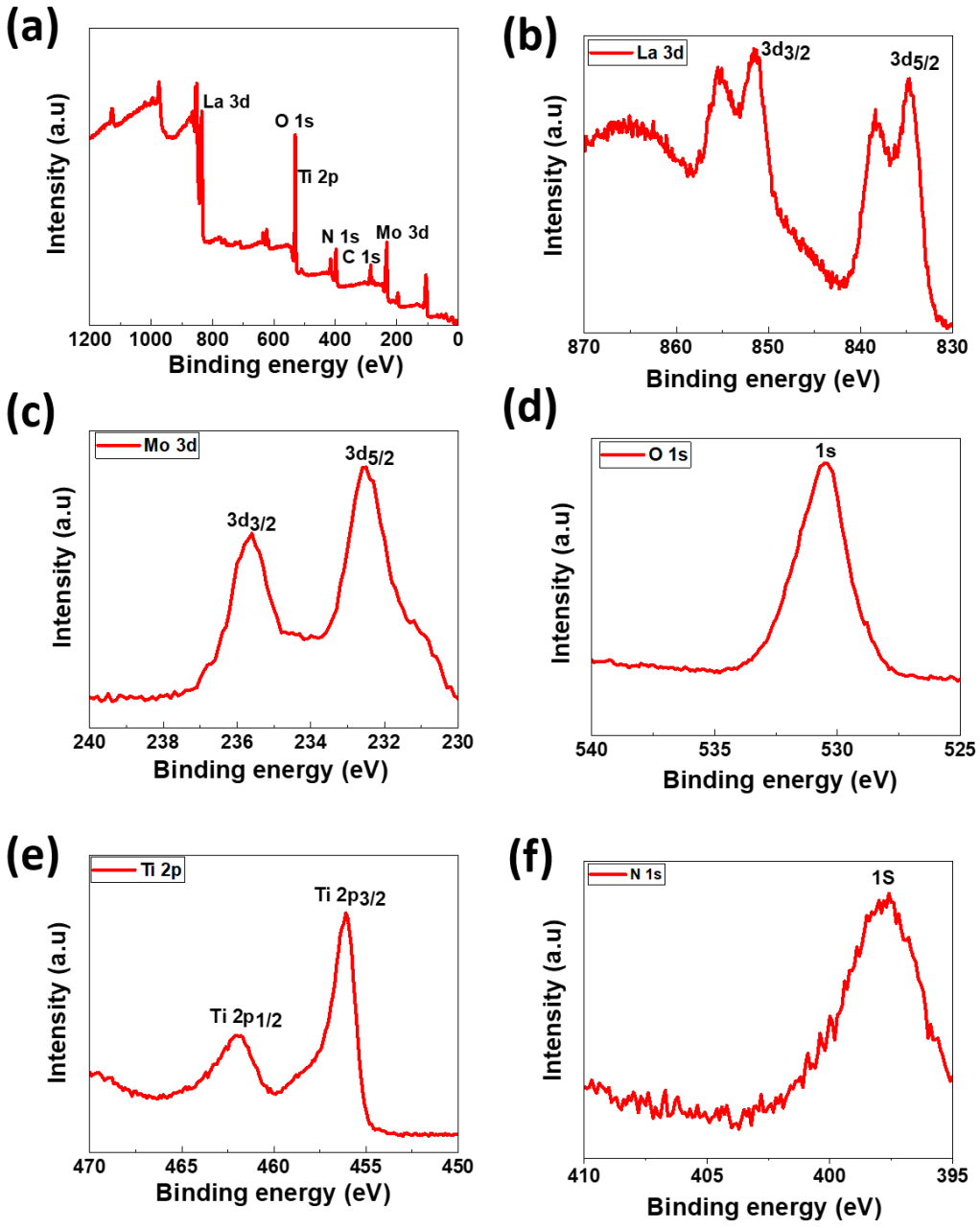

Figure 29. XPS spectra of $LaMo(ON)_x/TiO_2$ heterostructure: (a) XPS survey spectra and the high resolution XPS spectra of (b) La 3d (c) of Mo 3d (d) O 1s (e) Ti 2p and (f) N 1s

4.6. Photoelectrochemical performance

Electrochemical measurements were investigated to acquire the information about the PEC performance of the TiO_2 heterojunctions. Figure 30a demonstrates linear

sweep voltammograms of pure TiO_2 and TiO_2/$LaMo(ON)_x$ in 1 M KOH solution under illumination with simulated sunlight. The heterostructure revealed higher current densities and lower onset potential (0.81 V vs. Ag/AgCl) compared to pure TiO_2 NRs (0.86 V vs. Ag/AgCl). Figure 30b demonstrates Tafel slope for pristine TiO_2 and TiO_2/$LaMo(ON)_x$. The reaction kinetics were evaluated by calculating the Tafel slopes. The calculated Tafel slope values for both electrodes were 0.67 and 0.58 V $decade^{-1}$ for TiO_2 and TiO_2/$LaMo(ON)_x$, respectively. Which affirms the acceleration in the charge transfer rate and the enhanced oxygen evolution reaction (OER) kinetics of the heterostructure compared to pure TiO_2[122]. To further confirm the enhanced PEC activity of TiO_2/$LaMo(ON)_x$ heterostructure compared to the pure TiO_2, the electrochemical impedance spectroscopy measurements were investigated. (EIS) is nondestructive technique and it was employed to obtain in depth understanding of the PEC performance and it was tested under the light illumination in frequency range 10^{-2}-10^5 Hz with 5 mV amplitude. Figure 30c demonstrates the Nyquist plot in the form of variation of imaginary part of impedance (Z") with the real analogy (Z'), the EIS Nyquist plot exhibits only one large arc resistance semicircle for pristine TiO_2 and smaller semicircle for the heterostructure. The larger arc radius resistance was achieved for the pristine TiO_2 compared to the smaller arc radius resistance of the $LaMo(ON)_x$/TiO_2, which was obtained due to the dramatic reduction in the charge transfer resistance to the electrode-electrolyte interface after the deposition of $LaMo(ON)_x$ on the TiO_2 NRs arrays. The smaller the radius, the lower the charge transfer impedance at the electrode-electrolyte interface[98]. Under the light illumination, the $LaMo(ON)_x$/TiO_2 shows higher photocurrent density than the pristine TiO_2 at 0.8 V versus Ag/AgCl, which corresponds to the chronoamperometry experimental results. The chronoamperometric *i-t* curves were recorded upon intermittent light irradiation

(on-off) (Figure 30d). Because of the chopped light illumination, the samples show around zero current in the dark environment and after the light illumination, a transient increase is observed, which verify the good photoresponse. As it can be observed from Figure 30d, the heterostructure of TiO_2 exhibits higher photocurrent density (3.75 mA cm^{-2}) than the pristine TiO_2 (1.68 mA cm^{-2}), which verify the suitable combination of $LaMo(ON)_x$ with TiO_2 NRs. The PEC performance increased by around the double as high as that of the pristine TiO_2 NRs under simulate one-sun illumination. However, the sharp decrease shown in the photocurrent density of the heterostructure at the first cycle is due to the carrier recombination rate according to Kamat[123].

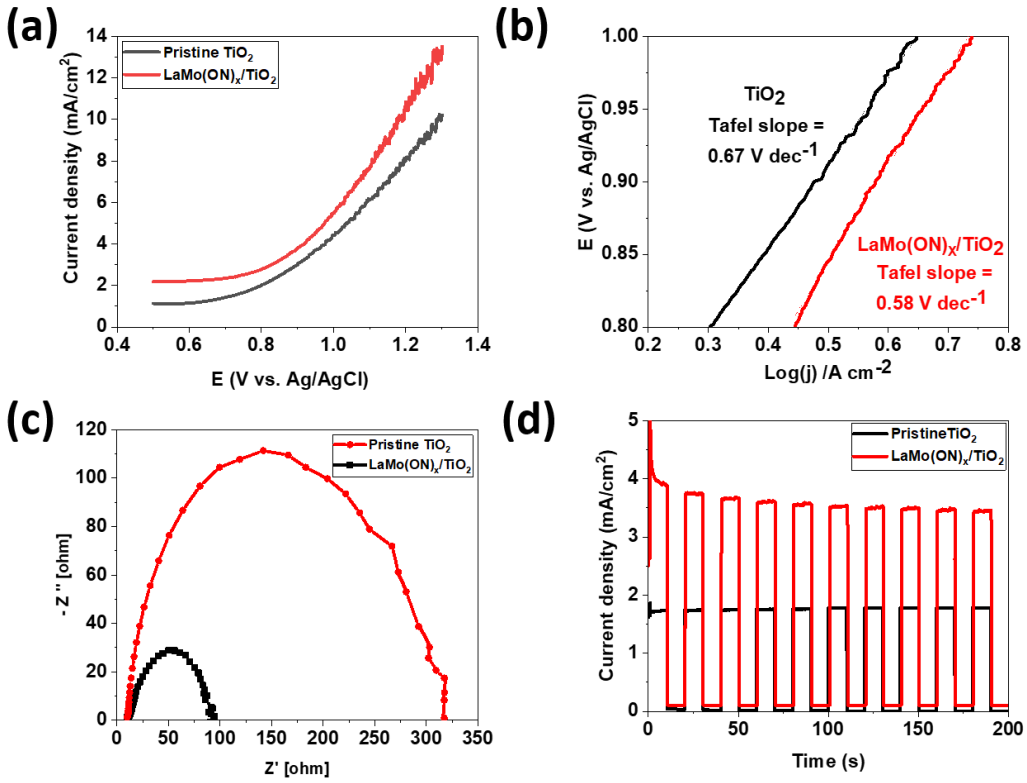

Figure 30. (a) The linear sweep voltammograms of pristine TiO_2 and $LaMo(ON)_x/TiO_2$ (b) Tafel plots of TiO_2 and $LaMo(ON)_x/TiO_2$ (c) Nyquist impedance plots of TiO_2 and $LaMo(ON)_x/TiO_2$ recorded at 0.8 V vs. Ag/AgCl in 1 M KOH. (d) Amperometric on-off curve of TiO_2 and $LaMo(ON)_x/TiO_2$ at 0.8 V vs Ag/AgCl with light on/off cycles

Figure 31 represents the Bode phase plots based on the following relation to calculate the interfacial electron recombination time:

$$\tau_n=(1/2\pi f_{max})$$

The longer τ_n value, the slower interfacial electron recombination and more trapping density[124]. The characteristic peak frequency shifts to a lower value for the heterostructure as represented in Bode phase plot (Figure 31). As a result, the heterostructure exhibits longer electron lifetime compared to the pristine TiO_2.

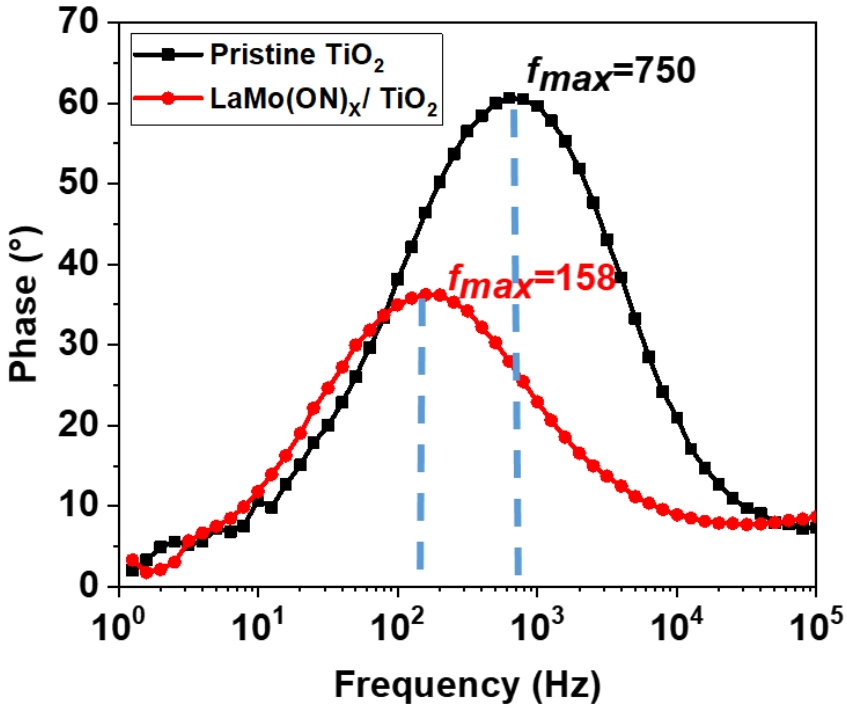

Figure 31. (a) Bode phase plot of pristine TiO_2 and $LaMo(ON)_x/TiO_2$

The longer lifetime of the photogenerated charges in the heterojunction system could be because the heterojunction separates the photoexcited electrons and holes efficiently.

Table6. The Maximum Frequency and Electron Life Time of TiO_2 and $LaMo(ON)_x/TiO_2$.

Sample	**f_{max}**	**τ_n**
TiO_2	750 Hz	0.21 ms
$LaMo(ON)_x/TiO_2$	158 Hz	1.01 ms

The energy bands of TiO_2 and $LaMo(ON)_x$ are schematically shown in Figure 32 and a mechanism depicting the movement of the photogenerated charge transfers is illustrated.

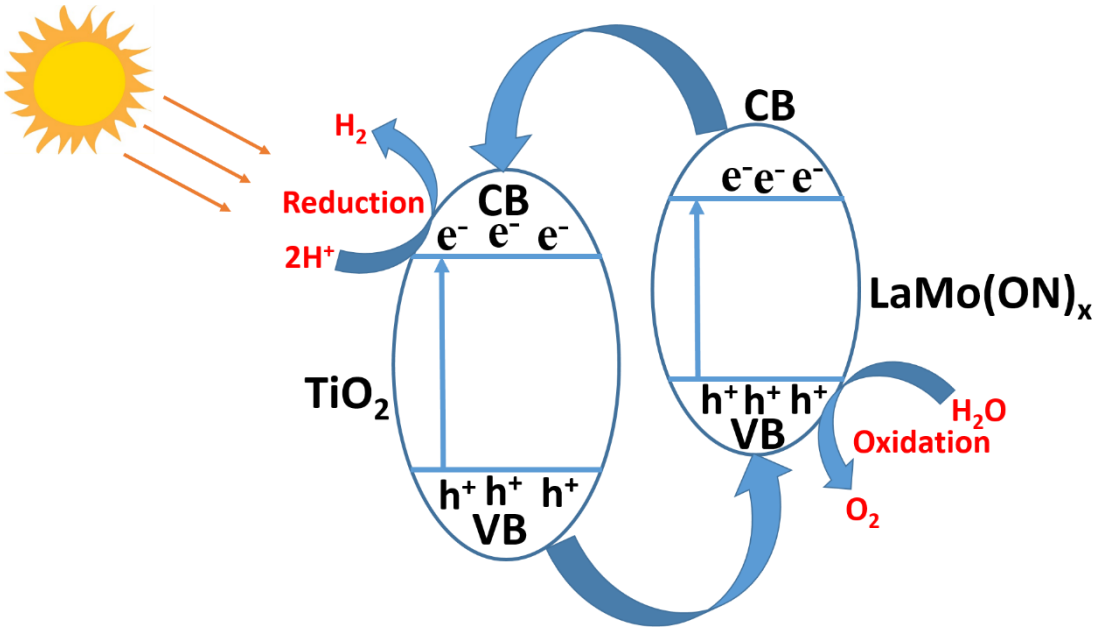

Figure 32. Schematic diagram photocatalytic mechanism of the $LaMo(ON)_x/TiO_2$ heterostructure under light

The experimental results demonstrated that the energy bands of $LaMo(ON)_x$ have a good alignment with TiO_2 to construct the indicated heterojunction. The appropriate band alignment allows the charges transfer from one semiconductor to

another[125]. After the illumination of light, the valance electrons of $LaMo(ON)_x$ will be excited to the CB, and the holes will be generated. Then, the electrons migrate from the CB of $LaMo(ON)_x$ to the CB of TiO_2 to initiate the reduction reaction of the H^+ ions to form the H_2 gas. However, the holes migrate from VB of TiO_2 to VB of $LaMo(ON)_x$ where the oxidation reaction of water takes place to produce the O_2 gas. As a consequence, the formation of a semiconductor-semiconductor heterojunction results in longer e^--h^+ charges lifetime, which reduces the photogenerated charges recombination rate to produce better photocatalytic activity than pristine TiO_2 or $LaMo(ON)_x$.

CHAPTER 5: CONCLUSION

The fabricated novel heterostructure $LaMo(ON)_x/TiO_2$ NRs arrays introduces a heterojunction system that was not reported in the literature before. After the preparation of the as-fabricated TiO_2 NRs on the FTO/glass substrate using hydrothermal synthesis, $LaMo(ON)_x$ have been deposited on the TiO_2 NRs by electrophoretic deposition. The experimental characterization results revealed the formation of the heterostructure by the coupling with the TiO_2 NRs. The SEM images showed a homogenous well covering of the $LaMo(ON)_x$ particles on the TiO_2 NRs. The X-ray diffraction of the heterostructure showed the characteristic rutile XRD peaks and the peaks of the $LaMo(ON)_x$, which is a structural evidence of the heteostructure formation. Raman spectroscopy signified that the main Raman peaks showed a shift in the peak position which confirms the new phase formation of the $LaMo(ON)_x/TiO_2$ heterostructure. The photocatalytic activity of the $LaMo(ON)_x/TiO_2$ heterostructure showed higher photocurrent density of more than two times than the pristine TiO_2 NRs, which confirms the enhancement of the PEC performance. The EIS showed lower charge transfer resistance, and longer photogenerated electron lifetime for the $LaMo(ON)_x/TiO_2$ compared to the pristine TiO_2. The improvement of the photocatalytic activity of the $LaMo(ON)_x/TiO_2$ could be due to the rapid and efficient charges transfer and the longer electron lifetime that decreases the photogenerated charges recombination rate. The new heterojunction system provides several advantages of the efficient e-h separation, faster charge transfer, and longer electron lifetime, which are the main reasons behind the enhanced PEC performance. The $LaMo(ON)_x/TiO_2$ heterostructure is used for efficient solar driven water splitting by enhancing the photocatalytic performance of TiO_2 NRs through coupling it with $LaMo(ON)_x$ via a simple deposition technique.

FUTURER WORK

TiO_2 heterojunction is attracting a lot of interest due to its ability to enhance the photocatalytic performance of the TiO_2, which can be used in several applications. The novel $LaMo(ON)_x$ material can be coupled efficiently with TiO_2 NRs to achieve improved photocatalytic activity. In the future, several strategies could be tested to obtain more remarkable improvements such as the formation of the heterostructure using different deposition techniques, synthesizing $LaMo(ON)_x$ material with different morphological shapes (nanoflakes, nanorodes, nanobelts…..etc). It is interesting to study the effect of deposited thickness of the $LaMo(ON)_x$ material on the TiO_2. This work evidenced that coupling TiO_2 with other materials (such as oxynitride) is a promising method to enhance PEC performance.

REFERENCES

1. Hosseini, S. E. & Wahid, M. A. Hydrogen production from renewable and sustainable energy resources: Promising green energy carrier for clean development. *Renew. Sustain. Energy Rev.* **57**, 850–866 (2016).
2. Reddy, P. J. *Solar Power Generation: Technology, New Concepts & Policy*. (CRC Press, 2012).
3. Lewis, N. S. & Crabtree, G. *Basic research needs for solar energy utilization*. *Workshop on solar enegy utilization* (2005).
4. Walter, M. G. *et al.* Solar water splitting cells. *Chem. Rev.* **110**, 6446–6473 (2010).
5. Chen, Z., Dinh, H. N. & Miller, E. *Photoelectrochemical Water Splitting - Standards, Experimental Methods, and Protocols*. *Springer Briefs in Energy* (2013). doi:10.1021/jm101179e
6. Agbenyega, J. Hydrogen generation. *Materials Today* **13**, 10 (2010).
7. Eftekhari, A., Babu, V. J. & Ramakrishna, S. Photoelectrode nanomaterials for photoelectrochemical water splitting. *Int. J. Hydrogen Energy* **42**, 11078–11109 (2017).
8. Japan Atomic Energy Agency. Hydrogen Society in the Future. Available at: https://www.jaea.go.jp/04/o-arai/nhc/en/data/data_10.html.
9. Bak, T., Nowotny, J., Rekas, M. & Sorrell, C. C. Photo-electrochemical hydrogen generation from water using solar energy. Materials-related aspects. *Int. J. Hydrogen Energy* **27**, 991–1022 (2002).
10. Kittel, C. *Introduction to Solid State Physics*. (Wiley, 2004).
11. The absolute electrode potential: an explanatory note (Recommendations 1986) . *Pure and Applied Chemistry* **58**, 955 (1986).

12. Weber, M. F. & Dignam, M. J. Splitting water with semiconducting photoelectrodes Efficiency considerations. *Int. J. Hydrogen Energy* **11**, 225–232 (1986).

13. Bolton, J. R., Strickler, S. J. & Connolly, J. S. Limiting and realizable efficiencies of solar photolysis of water. *Nature* **316**, 495–500 (1985).

14. Vayssieres, L. *On Solar Hydrogen and Nanotechnology*. (Wiley, 2010).

15. Maeda, K. & Domen, K. Photocatalytic Water Splitting: Recent Progress and Future Challenges. *J. Phys. Chem. Lett.* **1**, 2655–2661 (2010).

16. Maeda, K. Photocatalytic water splitting using semiconductor particles: History and recent developments. *J. Photochem. Photobiol. C Photochem. Rev.* **12**, 237–268 (2011).

17. Benck, J. D., Pinaud, B. A., Gorlin, Y. & Jaramillo, T. F. Substrate Selection for Fundamental Studies of Electrocatalysts and Photoelectrodes: Inert Potential Windows in Acidic, Neutral, and Basic Electrolyte. *PLoS One* **9**, e107942 (2014).

18. Krol, R. van de & Grätzel, M. *Photoelectrochemical Hydrogen Production*. **102**, (Springer US, 2012).

19. Sivula, K. & van de Krol, R. Semiconducting materials for photoelectrochemical energy conversion. *Nat. Rev. Mater.* **1**, 15010 (2016).

20. Chen, X. *et al.* Recent advances in visible-light-driven photoelectrochemical water splitting: Catalyst nanostructures and reaction systems. *Nano-Micro Lett.* **8**, 1–12 (2016).

21. Khan, S. U. M., Al-Shahry, M. & Ingler, W. B. Efficient Photochemical Water Splitting by a Chemically Modified n-TiO_2. *Science (80-.).* **297**, 2243 LP – 2245 (2002).

22. Guo, Z., Ma, R. & Li, G. Degradation of phenol by nanomaterial TiO_2 in wastewater. *Chem. Eng. J.* **119**, 55–59 (2006).

23. Yu, J., Fan, J. & Lv, K. Anatase TiO_2 nanosheets with exposed (001) facets: improved photoelectric conversion efficiency in dye-sensitized solar cells. *Nanoscale* **2**, 2144–2149 (2010).

24. Meinhold, G. Rutile and its applications in earth sciences. *Earth-Science Rev.* **102**, 1–28 (2010).

25. Diebold, U. The surface science of titanium dioxide. *Surf. Sci. Rep.* **48**, 53–229 (2003).

26. Ranade, M. R. *et al.* Energetics of nanocrystalline TiO_2. *Proc. Natl. Acad. Sci.* **99**, 6476 LP – 6481 (2002).

27. Science, N. & Mascaretti, L. Hydrogen-treated titanium dioxide hierarchical nanostructures for water splitting applications. (2017).

28. Hanaor, D. A. H. & Sorrell, C. C. Review of the anatase to rutile phase transformation. *J. Mater. Sci.* **46**, 855–874 (2011).

29. Tang, H., Prasad, K., Sanjinès, R., Schmid, P. E. & Lévy, F. Electrical and optical properties of TiO_2 anatase thin films. *J. Appl. Phys.* **75**, 2042–2047 (1994).

30. Koelsch, M., Cassaignon, S., Guillemoles, J. F. & Jolivet, J. P. Comparison of optical and electrochemical properties of anatase and brookite TiO_2 synthesized by the sol–gel method. *Thin Solid Films* **403**–**404**, 312–319 (2002).

31. Cronemeyer, D. C. Electrical and Optical Properties of Rutile Single Crystals. *Phys. Rev.* **87**, 876–886 (1952).

32. Landmann, M., Rauls, E. & Schmidt, W. G. The electronic structure and optical response of rutile, anatase and brookite TiO_2. *J. Phys. Condens. Matter* **24**,

195503 (2012).

33. Hwang, Y. J., Hahn, C., Liu, B. & Yang, P. Photoelectrochemical Properties of TiO_2 Nanowire Arrays: A Study of the Dependence on Length and Atomic Layer Deposition Coating. *ACS Nano* **6**, 5060–5069 (2012).

34. Etacheri, V., Di Valentin, C., Schneider, J., Bahnemann, D. & Pillai, S. C. Visible-light activation of TiO_2 photocatalysts: Advances in theory and experiments. *J. Photochem. Photobiol. C Photochem. Rev.* **25**, 1–29 (2015).

35. Kumar, S. G. & Devi, L. G. Review on modified TiO_2 photocatalysis under UV/visible light: Selected results and related mechanisms on interfacial charge carrier transfer dynamics. *J. Phys. Chem. A* **115**, 13211–13241 (2011).

36. Shen, S. *et al.* Titanium dioxide nanostructures for photoelectrochemical applications. *Prog. Mater. Sci.* **98**, 299–385 (2018).

37. Fang, W., Xing, M. & Zhang, J. Modifications on reduced titanium dioxide photocatalysts: A review. *J. Photochem. Photobiol. C Photochem. Rev.* **32**, 21–39 (2017).

38. Zhang, J., Xiao, G., Xiao, F.-X. & Liu, B. Revisiting one-dimensional TiO_2 based hybrid heterostructures for heterogeneous photocatalysis: a critical review. *Mater. Chem. Front.* **1**, 231–250 (2017).

39. Qi, W. *et al.* Hydrothermal synthesis of TiO_2 nanorods arrays on ITO. *Mater. Chem. Phys.* **207**, 435–441 (2018).

40. Grimes, C. A. & Mor, G. K. *TiO_2 Nanotube Arrays*. (Springer US, 2009). doi:10.1007/978-1-4419-0068-5

41. Hussian, H. A. R. A., Hassan, M. A. M. & Agool, I. R. Synthesis of titanium dioxide (TiO_2) nanofiber and nanotube using different chemical method. *Optik (Stuttg).* **127**, 2996–2999 (2016).

42. Han, X., Kuang, Q., Jin, M., Xie, Z. & Zheng, L. Synthesis of Titania Nanosheets with a High Percentage of Exposed (001) Facets and Related Photocatalytic Properties. *J. Am. Chem. Soc.* **131**, 3152–3153 (2009).

43. Wang, Y. *et al.* Visible light driven type II heterostructures and their enhanced photocatalysis properties: A review. *Nanoscale* **5**, 8326–8339 (2013).

44. Zhou, W. *et al.* Synthesis of few-layer MoS_2 nanosheet-coated TiO_2 nanobelt heterostructures for enhanced photocatalytic activities. *Small* **9**, 140–147 (2013).

45. Zhao, D. *et al.* Surface Modification of TiO_2 by Phosphate: Effect on Photocatalytic Activity and Mechanism Implication. *J. Phys. Chem. C* **112**, 5993–6001 (2008).

46. Boullosa-Eiras, S. *et al.* Catalytic hydrodeoxygenation (HDO) of phenol over supported molybdenum carbide, nitride, phosphide and oxide catalysts. *Catal. Today* **223**, 44–53 (2014).

47. Devi, L. G., Murthy, B. N. & Kumar, S. G. Photocatalytic activity of TiO_2 doped with $Zn^{2+}$and V^{5+}transition metal ions: Influence of crystallite size and dopant electronic configuration on photocatalytic activity. *Mater. Sci. Eng. B Solid-State Mater. Adv. Technol.* **166**, 1–6 (2010).

48. Liang, R., Hu, A., Persic, J. & Zhou, Y. N. Palladium Nanoparticles Loaded on Carbon Modified TiO_2 Nanobelts for Enhanced Methanol Electrooxidation Citation. *Nano-Micro Lett* **5**, 202–212 (2013).

49. Hwang, Y. J., Yang, S. & Lee, H. Surface analysis of N-doped TiO_2 nanorods and their enhanced photocatalytic oxidation activity. *Appl. Catal. B Environ.* **204**, 209–215 (2017).

50. Ibarra-Rodriguez, L. I., Huerta-Flores, A. M. & Torres-Martínez, L. M. Facile synthesis of g-C_3N_4/ $LaMO_3$ (M: Co, Mn, Fe) composites for enhanced visible-

light-driven photocatalytic water splitting. *Mater. Sci. Semicond. Process.* **103**, 104643 (2019).

51. Seo, J. *et al.* Solar-Driven Water Splitting over a $BaTaO_2N$ Photoanode Enhanced by Annealing in Argon. *ACS Appl. Energy Mater.* **2**, 5777–5784 (2019).

52. Hojamberdiev, M. & Kawashima, K. Exploring flux-grown transition metal oxynitride perovskites for photocatalytic water oxidation: A minireview. *Energy Reports* (2019). doi:10.1016/j.egyr.2019.09.021

53. Low, J., Yu, J., Jaroniec, M., Wageh, S. & Al-Ghamdi, A. A. Heterojunction Photocatalysts. *Adv. Mater.* **29**, (2017).

54. Zhang, L. & Jaroniec, M. Toward designing semiconductor-semiconductor heterojunctions for photocatalytic applications. *Appl. Surf. Sci.* **430**, 2–17 (2018).

55. FUJISHIMA, A. & HONDA, K. Electrochemical Photolysis of Water at a Semiconductor Electrode. *Nature* **238**, 37 (1972).

56. Saraswat, S. K., Rodene, D. D. & Gupta, R. B. Recent advancements in semiconductor materials for photoelectrochemical water splitting for hydrogen production using visible light. *Renew. Sustain. Energy Rev.* **89**, 228–248 (2018).

57. Garay-Rodríguez, L. F., Yoshida, H. & Torres-Martínez, L. M. Flux synthesis of $Ba_2Li_2/3Ti1_6/3O_{13}$ and its photocatalytic performance. *Dalt. Trans.* **48**, 12105–12115 (2019).

58. Liu, B. & Aydil, E. S. Growth of oriented single-crystalline rutile TiO_2 nanorods on transparent conducting substrates for dye-sensitized solar cells. *J. Am. Chem. Soc.* **131**, 3985–3990 (2009).

59. Onishi, T., Teranishi, M., Naya, S., Fujishima, M. & Tada, H. Electrocatalytic

Effect on the Photon-to-Current Conversion Efficiency of Gold-Nanoparticle-Loaded Titanium(IV) Oxide Plasmonic Electrodes for Water Oxidation. *J. Phys. Chem. C* **124**, 6103–6109 (2020).

60. He, S. *et al.* Hierarchical Ta-Doped TiO_2 Nanorod Arrays with Improved Charge Separation for Photoelectrochemical Water Oxidation under FTO Side Illumination. *Nanomaterials* **8**, 983 (2018).

61. Rangel-Vázquez, I. *et al.* Synthesis and characterization of Sn doped TiO_2 photocatalysts: Effect of Sn concentration on the textural properties and on the photocatalytic degradation of 2,4-dichlorophenoxyacetic acid. *J. Alloys Compd.* **643**, S144–S149 (2015).

62. Mehraz, S., Kongsong, P., Taleb, A., Dokhane, N. & Sikong, L. Large scale and facile synthesis of Sn doped TiO_2 aggregates using hydrothermal synthesis. *Sol. Energy Mater. Sol. Cells* **189**, 254–262 (2019).

63. Chebout, A. A. and F. B. and M. B. and R. T.-I. and M. T. and F. K. and K. Effect of Er doping on the microstructural, optical, and photocatalytic activity of TiO_2 thin films. *Mater. Res. Express* **6**, 16406 (2019).

64. Eadi, S. B., Kim, S., Jeong, S. W. & Jeon, H. W. Novel Preparation of Fe Doped TiO_2 Nanoparticles and Their Application for Gas Sensor and Photocatalytic Degradation. *Adv. Mater. Sci. Eng.* **2017**, (2017).

65. Primc, D. *et al.* Doping of TiO_2 as a tool to optimize the water splitting efficiencies of titania-hematite photoanodes. *Sustain. Energy Fuels* **1**, 199–206 (2017).

66. Kunnamareddy, M., Diravidamani, B., Rajendran, R., Singaram, B. & Varadharajan, K. Synthesis of silver and sulphur codoped TiO_2 nanoparticles for photocatalytic degradation of methylene blue. *J. Mater. Sci. Mater. Electron.* **29**,

18111–18119 (2018).

67. Aragaw, B. A. *et al.* Facile one-pot controlled synthesis of Sn and C codoped single crystal TiO_2 nanowire arrays for highly efficient photoelectrochemical water splitting. *Appl. Catal. B Environ.* **163**, 478–486 (2015).

68. Li, T. & Ding, D. Ni/Si-Codoped TiO_2 Nanostructure Photoanode for Enhanced Photoelectrochemical Water Splitting. *Materials (Basel).* **12**, 4102 (2019).

69. Zhang, X., Zhang, B., Zuo, Z., Wang, M. & Shen, Y. N/Si co-doped oriented single crystalline rutile TiO_2 nanorods for photoelectrochemical water splitting. *J. Mater. Chem. A* **3**, 10020–10025 (2015).

70. Humayun, M., Raziq, F., Khan, A. & Luo, W. Modification strategies of TiO_2 for potential applications in photocatalysis: A critical review. *Green Chem. Lett. Rev.* **11**, 86–102 (2018).

71. Jeong, K., Deshmukh, P. R., Park, J., Sohn, Y. & Shin, W. G. ZnO-TiO_2 Core–Shell Nanowires: A Sustainable Photoanode for Enhanced Photoelectrochemical Water Splitting. *ACS Sustain. Chem. Eng.* **6**, 6518–6526 (2018).

72. Zhang, G., Tan, Y., Sun, Z. & Zheng, S. Synthesis of BiOCl/TiO_2 heterostructure composites and their enhanced photocatalytic activity. *J. Environ. Chem. Eng.* **5**, 1196–1204 (2017).

73. Tian, J. *et al.* RuO_2/TiO_2 nanobelt heterostructures with enhanced photocatalytic activity and gas-phase selective oxidation of benzyl alcohol. *Sol. Energy Mater. Sol. Cells* **151**, 7–13 (2016).

74. Mousli *et al.* Polyaniline-Grafted RuO_2-TiO_2 Heterostructure for the Catalysed Degradation of Methyl Orange in Darkness. *Catalysts* **9**, 578 (2019).

75. Mei, Q. *et al.* TiO_2/Fe_2O_3 heterostructures with enhanced photocatalytic reduction of Cr(vi) under visible light irradiation. *RSC Adv.* **9**, 22764–22771

(2019).

76. Nam Trung, T., Kamand, F. Z. & Al tahtamouni, T. M. Elucidating the mechanism for the chemical vapor deposition growth of vertical MoO_2/MoS_2 flakes toward photoelectrochemical applications. *Appl. Surf. Sci.* **505**, (2020).

77. Lai, C. W., Lau, K. S. & Chou, P. M. $CdSe/TiO_2$ nanotubes for enhanced photoelectrochemical activity under solar illumination: Influence of soaking time in CdSe bath solution. *Chem. Phys. Lett.* **714**, 6–10 (2019).

78. Tian, J., Hao, P., Wei, N., Cui, H. & Liu, H. 3D Bi_2MoO_6 Nanosheet/TiO_2 Nanobelt Heterostructure: Enhanced Photocatalytic Activities and Photoelectochemistry Performance. *ACS Catal.* **5**, 4530–4536 (2015).

79. Wang, S., Liu, G. & Wang, L. Crystal Facet Engineering of Photoelectrodes for Photoelectrochemical Water Splitting. *Chem. Rev.* **119**, 5192–5247 (2019).

80. Kumar, V. *et al.* Properties and performance of photocatalytic CeO2, TiO_2, and CeO_2–TiO_2 layered thin films. *Ceram. Int.* **45**, 22085–22094 (2019).

81. Tian, J. *et al.* Enhanced photocatalytic performances of CeO_2/TiO_2 nanobelt heterostructures. *Small* **9**, 3864–3872 (2013).

82. Li, W., Liu, X. & Li, H. Hydrothermal synthesis of graphene/Fe^{3+}-doped TiO_2 nanowire composites with highly enhanced photocatalytic activity under visible light irradiation. *J. Mater. Chem. A* **3**, 15214–15224 (2015).

83. Lou, X.-W. D. Fabrication of Heterostructured Fe_2TiO_5-TiO_2 Nanocages with Enhanced Photoelectrochemical Performance for Solar Energy Conversion. *Angew. Chemie Int. Ed.* (2020). doi:10.1002/anie.202000697

84. Huang, X., Zhao, G., Wang, G. & Irvine, J. T. S. Synthesis and applications of nanoporous perovskite metal oxides. *Chem. Sci.* **9**, 3623–3637 (2018).

85. Okamoto, H. *et al.* Effects of annealing conditions on the oxygen evolution

activity of a $BaTaO_2N$ photocatalyst loaded with cobalt species. *Catal. Today* (2018). doi:https://doi.org/10.1016/j.cattod.2018.12.048

86. Jian, Z., Huang, S., Cao, Y. & Zhang, Y. Hydrothermal Preparation and Characterization of $TiO_2/BiVO_4$ Composite Catalyst and its Photolysis of Water to Produce Hydrogen. *Photochem. Photobiol.* **92**, 363–370 (2016).

87. Nasr, M. *et al.* Synthesis of $BiOF/TiO_2$ Heterostructures and Their Enhanced Visible-Light Photocatalytic Activity. *Eur. J. Inorg. Chem.* **2020**, 253–260 (2020).

88. Hernández, S. *et al.* Optimization of 1D $ZnO@TiO_2$ core-shell nanostructures for enhanced photoelectrochemical water splitting under solar light illumination. *ACS Appl. Mater. Interfaces* **6**, 12153–12167 (2014).

89. Liu, Q. *et al.* 2D $ZnIn_2S_4$ Nanosheet/1D TiO_2 Nanorod heterostructure arrays for improved photoelectrochemical water splitting. *ACS Appl. Mater. Interfaces* **6**, 17200–17207 (2014).

90. Wei, N. *et al.* Construction of noble-metal-free TiO_2 nanobelt/$ZnIn_2S_4$ nanosheet heterojunction nanocomposite for highly efficient photocatalytic hydrogen evolution. *Nanotechnology* **30**, 045701 (2019).

91. Tian, J. *et al.* Enhanced performance of CdS/CdSe quantum dot cosensitized solar cells via homogeneous distribution of quantum dots in TiO_2 film. *J. Phys. Chem. C* **116**, 18655–18662 (2012).

92. Li, Y. *et al.* Achieving Controllable $CoTiO_3$-Encapsulated TiO_2 Heterostructures for Enhanced Photoelectrochemical Water Splitting. 3–9 (2019). doi:10.1021/acsaem.9b01694

93. Wan, L. *et al.* Achieving photocatalytic water oxidation on $LaNbON_2$ under visible light irradiation. *J. Energy Chem.* **27**, 367–371 (2018).

94. Jadhav, S. *et al.* Efficient photocatalytic oxygen evolution using $BaTaO_2N$ obtained from nitridation of perovskite-type oxide. *J. Mater. Chem. A* **8**, 1127–1130 (2020).

95. Liu, B. & Aydil, E. S. Growth of Oriented Single-Crystalline Rutile TiO_2 Nanorods on Transparent Conducting Substrates for Dye-Sensitized.pdf. 3985–3990 (2009).

96. Zhang, Q. Z. *et al.* Synthesis of spherical $La_2Mo_2O_9$ nanoparticles using sol-gel process. *Adv. Mater. Res.* **933**, 8–11 (2014).

97. *Advances in Photoelectrochemical Water Splitting*. (Royal Society of Chemistry, 2018). doi:10.1039/9781782629863

98. Lasia, A. *Electrochemical Impedance Spectroscopy and its Applications*. (Springer New York, 2014). doi:10.1007/978-1-4614-8933-7

99. Egerton, R. F. *Physical Principles of Electron Microscopy*. (Springer International Publishing, 2016). doi:10.1007/978-3-319-39877-8

100. Smith, E. & Dent, G. *Modern Raman Spectroscopy - A Practical Approach*. (John Wiley & Sons, Ltd, 2004). doi:10.1002/0470011831

101. Bührer, W. & Brüesch, P. *Phonons: Theory and Experiments II: Experiments and Interpretation of Experimental Results*. (Springer Berlin Heidelberg, 2012).

102. Lupoi, J. S. Developments in enzyme immobilization and near-infrared Raman spectroscopy with downstream renewable energy applications. (Iowa State University, Digital Repository, 2012). doi:10.31274/etd-180810-1310

103. Waseda, Y., Matsubara, E. & Shinoda, K. *X-Ray Diffraction Crystallography*. (Springer Berlin Heidelberg, 2011). doi:10.1007/978-3-642-16635-8

104. Russell, J. & Cohn, R. *Miller Index*. (Book on Demand, 2012).

105. van der Heide, P. *X-Ray Photoelectron Spectroscopy*. (John Wiley & Sons, Inc.,

2011). doi:10.1002/9781118162897

106. Scanning X-ray Photoelectron Spectrometer (XPS). Available at: https://engineering.virginia.edu/research/facilities/nanoscale-materials-characterization-facility/instrumentation/x-ray-3.

107. Moulder, J. F. & Chastain, J. *Handbook of X-ray Photoelectron Spectroscopy: A Reference Book of Standard Spectra for Identification and Interpretation of XPS Data*. (Physical Electronics Division, Perkin-Elmer Corporation, 1992).

108. Buchholz, D. B., Liu, J., Marks, T. J., Zhang, M. & Chang, R. P. H. Control and Characterization of the Structural, Electrical, and Optical Properties of Amorphous Zinc−Indium−Tin Oxide Thin Films. *ACS Appl. Mater. Interfaces* **1**, 2147–2153 (2009).

109. Muniz, F. T. L., Miranda, M. A. R., Morilla dos Santos, C. & Sasaki, J. M. The Scherrer equation and the dynamical theory of X-ray diffraction. *Acta Crystallogr. Sect. A Found. Adv.* **72**, 385–390 (2016).

110. Lima, F. M., Martins, F. M., Maia Júnior, P. H. F., Almeida, A. F. L. & Freire, F. N. A. Nanostructured titanium dioxide average size from alternative analysis of Scherrer's Equation. *Matéria (Rio Janeiro)* **23**, (2018).

111. Deo, G. *et al.* Physical and chemical characterization of surface vanadium oxide supported on titania: influence of the titania phase (anatase, rutile, brookite and B). *Appl. Catal. A Gen.* **91**, 27–42 (1992).

112. Lukačević, I., Gupta, S. K., Jha, P. K. & Kirin, D. Lattice dynamics and Raman spectrum of rutile TiO_2: The role of soft phonon modes in pressure induced phase transition. *Mater. Chem. Phys.* **137**, 282–289 (2012).

113. Arsov, L. D., Kormann, C. & Plieth, W. Electrochemical synthesis and in situ Raman spectroscopy of thin films of titanium dioxide. *J. Raman Spectrosc.* **22**,

573–575 (1991).

114. Sekiya, T., Ohta, S., Kamei, S., Hanakawa, M. & Kurita, S. Raman spectroscopy and phase transition of anatase TiO_2 under high pressure. *J. Phys. Chem. Solids* **62**, 717–721 (2001).

115. Yan, J. *et al.* Understanding the effect of surface/bulk defects on the photocatalytic activity of TiO_2: anatase versus rutile. *Phys. Chem. Chem. Phys.* **15**, 10978–10988 (2013).

116. Zhang, Y., Harris, C. X., Wallenmeyer, P., Murowchick, J. & Chen, X. Asymmetric Lattice Vibrational Characteristics of Rutile TiO_2 as Revealed by Laser Power Dependent Raman Spectroscopy. *J. Phys. Chem. C* **117**, 24015–24022 (2013).

117. Swamy, V., Muddle, B. C. & Dai, Q. Size-dependent modifications of the Raman spectrum of rutile TiO2. *Appl. Phys. Lett.* **89**, 163118 (2006).

118. Porto, S. P. S., Fleury, P. A. & Damen, T. C. Raman spectra of TiO_2, MgF_2, ZnF_2, FeF_2, and MnF_2. *Phys. Rev.* **154**, 522–526 (1967).

119. McCafferty, E. & Wightman, J. P. Determination of the concentration of surface hydroxyl groups on metal oxide films by a quantitative XPS method. *Surf. Interface Anal.* **26**, 549–564 (1998).

120. Lance, R. Optical Analysis of Titania: Band Gaps of Brookite, Rutile and Anatase. 24 (2018).

121. Mahadik, M. A., Shinde, P. S., Lee, H. H., Cho, M. & Jang, J. S. Data on the effect of improved TiO_2/FTO interface and $Ni(OH)_2$ cocatalyst on the photoelectrochemical performances and stability of CdS cased $ZnIn_2S_4/TiO_2$ heterojunction. *Data Br.* **17**, 807–819 (2018).

122. Paul, K. K., Sreekanth, N., Biroju, R. K., Narayanan, T. N. & Giri, P. K. Solar

light driven photoelectrocatalytic hydrogen evolution and dye degradation by metal-free few-layer MoS_2 nanoflower/TiO_2(B) nanobelts heterostructure. *Sol. Energy Mater. Sol. Cells* **185**, 364–374 (2018).

123. Kongkanand, A., Tvrdy, K., Takechi, K., Kuno, M. & Kamat, P. V. Quantum Dot Solar Cells. Tuning Photoresponse through Size and Shape Control of CdSe−TiO_2 Architecture. *J. Am. Chem. Soc.* **130**, 4007–4015 (2008).

124. Bisquert, J., Fabregat-Santiago, F., Mora-Seró, I., Garcia-Belmonte, G. & Giménez, S. Electron Lifetime in Dye-Sensitized Solar Cells: Theory and Interpretation of Measurements. *J. Phys. Chem. C* **113**, 17278–17290 (2009).

125. Moniz, S. J. A., Shevlin, S. A., Martin, D. J., Guo, Z.-X. & Tang, J. Visible-light driven heterojunction photocatalysts for water splitting – a critical review. *Energy Environ. Sci.* **8**, 731–759 (2015).